



Titanium isotope systematics of refractory inclusions: Echoes of molecular cloud heterogeneity

Quinn R. Shollenberger^{a,b,*}, Jan Render^{b,1}, Michelle K. Jordan^{a,2},
Kaitlyn A. McCain^a, Samuel Ebert^b, Addi Bischoff^b, Thorsten Kleine^{b,3},
Edward D. Young^a

^a Department of Earth, Planetary, and Space Sciences, University of California Los Angeles, 595 Charles E Young Dr E, Los Angeles, CA 90095, USA

^b Institut für Planetologie, University of Münster, Wilhelm-Klemm-Straße 10, 48149 Münster, Germany

Received 1 March 2021; accepted in revised form 1 March 2022; Available online 5 March 2022

Abstract

Calcium-aluminum-rich inclusions (CAIs) are highly refractory objects found in different chondrite groups and represent some of the oldest known solids of the Solar System. As such, CAIs provide key information regarding the conditions prevailing in the solar protoplanetary disk as well as subsequent mixing and transport processes. Many studies have investigated CAIs for their isotopic compositions and reported nucleosynthetic isotope anomalies in numerous elements, which are typically explained by the variable incorporation of isotopically highly anomalous presolar phases. However, with the exception of ⁵⁴Cr-enriched nanospinel, the exact presolar phases responsible for the isotopic heterogeneities are yet to be identified. To address this issue, we here present *in-situ* Ti isotopic analyses obtained on a diverse set of CAIs from various CV3 chondrites. The *in-situ* measurements were performed by targeting individual mineral phases of 15 CAIs with laser-ablation mass spectrometry and indicate significant inter- and intra-CAI isotopic heterogeneity in the neutron-rich isotope ⁵⁰Ti. This is particularly pronounced for primitive fine-grained CAIs, whereas coarse-grained CAIs, which have been subject to melting, exhibit smaller degrees of Ti isotopic heterogeneity.

To further investigate this Ti isotopic heterogeneity, we additionally obtained Ti isotopic compositions of sequential acid leachates from two fine-grained and two coarse-grained CAIs derived from CV3 chondrites. In contrast to potential expectations from the first part of the study, we do not observe any significant intra-CAI Ti isotopic heterogeneity between the different leaching steps. The lack of intra-CAI Ti isotopic heterogeneity in the acid leachate samples of this study likely reflects that the leaching procedure is unable to efficiently separate the carriers of isotopically anomalous Ti in CAIs. By comparing the bulk CAI Ti isotope compositions with Ti isotope data for hibonite-rich objects from the literature, we find that the range of Ti isotope compositions recorded by CAIs from various chondrite groups can be accounted for by the averaging of hibonite grains. In turn, the variable Ti isotope compositions of hibonite grains can be explained by the averaging of isotopically diverse presolar grains present in the Sun's parental molecular cloud. This effect of averaging is statistically supported by the central limit theorem, and the concept has the potential to be useful for other isotopic systems.

© 2022 Elsevier Ltd. All rights reserved.

Keywords: Titanium isotopes; Refractory inclusions; Nucleosynthetic anomalies; Solar nebula; Early solar system

* Corresponding author at: Lawrence Livermore National Laboratory, 7000 East Ave, Livermore, CA 94550, USA.

E-mail address: shollenberger@llnl.gov (Q.R. Shollenberger).

¹ Lawrence Livermore National Laboratory, 7000 East Ave, Livermore, CA 94550, USA.

² Earth & Planets Laboratory, Carnegie Science, 5241 Broad Branch Road, NW, Washington, DC 20015, USA.

³ Max Planck Institute for Solar System Research, Justus-von-Liebig-Weg 3, 37077 Göttingen, Germany.

1. INTRODUCTION

Calcium-aluminum-rich inclusions (CAIs) are the oldest dated solids that formed within the Solar System near the young sun around 4.567 Ga (Amelin et al., 2010; Connelly et al., 2012). Therefore, these objects—and in particular their chemical and isotopic signatures—provide a window to examine the earliest reservoir(s) present in the Solar System and how that reservoir(s) evolved through time, a process critical for understanding the formation of later formed solids such as the terrestrial planets. Previous work has shown for a whole suite of elements that CAIs have mass-independent (nucleosynthetic) isotope anomalies compared to later formed Solar Systems solids (e.g., Dauphas and Schauble, 2016; Burkhardt et al., 2019 and references therein). More specifically, nucleosynthetic anomalies reported in CAIs and bulk meteorites demonstrate that CAIs are closely related to the carbonaceous (CC) meteorite reservoir (Burkhardt et al., 2019; Brennecka et al., 2020). This may, at first glance, seem surprising, as CAIs are commonly thought to have formed close to the young sun, whereas the CC reservoir was presumably located in the outer Solar System, beyond the orbit of Jupiter (Warren, 2011; Budde et al., 2016; Kruijjer et al., 2017). However, the isotopic link between CAIs and the CC reservoir results naturally through the outward transport of CAIs during rapid radial expansion of the early disk (Burkhardt et al., 2019; Nanne et al., 2019). This example highlights that understanding the history of CAIs is a key point in reconstructing Solar System formation and evolution.

Calcium-aluminum-rich refractory inclusions *sensu lato* can be divided into three different groups: (1) hibonite-rich inclusions, including platy hibonite crystals (PLACs) and spinel-hibonite inclusions (SHIBs), (2) CAIs that exhibit “Fractionated and Unidentified Nuclear” (FUN) isotopic anomalies, and (3) “normal” CAIs. Each of these groups is defined by certain isotopic characteristics, and hibonite-rich inclusions also differ from FUN and normal CAIs in terms of texture and mineralogy. For example, so-called normal CAIs can be categorized according to petrological characteristics; with coarse-grained CAIs exhibiting clear evidence of having been melted, whereas fine-grained CAIs have not been melted as indicated by their primitive texture and small grain sizes (generally < 10 μm). Type A CAIs are characterized by the presence of melilite and the absence of grossmanite and primary anorthite, while Type B CAIs have abundant primary anorthite and grossmanite (commonly referred to, but officially discredited, as ‘fassaite’). Fluffy Type A CAIs are irregular in shape, some comprising collections of “nodules”, and contain melilite and spinel in addition to perovskite (MacPherson and Grossman, 1984). Also, fluffy Type A CAIs are characterized by 60–75 volume percent of fine-grained, secondary alteration products. Isotopically, many of the normal CAIs have ^{26}Mg excesses consistent with the so-called canonical initial $^{26}\text{Al}/^{27}\text{Al}$ ratios (i.e., $\sim 5.2 \times 10^{-5}$; Jacobsen et al., 2008; MacPherson et al., 2012), and a small range of ^{50}Ti anomalies from ~ 2 to 15 in $\epsilon^{50}\text{Ti}$ units, where $\epsilon^{50}\text{Ti}$ is the parts per

ten thousand deviation relative to terrestrial $^{50}\text{Ti}/^{47}\text{Ti}$ after internal normalization, with a distinct peak near $\epsilon^{50}\text{Ti} = 9$ (e.g., Leya et al., 2009; Trinquier et al., 2009; Williams et al., 2016; Simon et al., 2017; Davis et al., 2018; Ebert et al., 2018; Render et al., 2019; Torrano et al., 2019). In comparison, hibonite-rich inclusions either lack clear evidence for ^{26}Al or have evidence for low initial $^{26}\text{Al}/^{27}\text{Al}$ ratios (e.g., Ireland, 1990; Liu et al., 2009, 2012; Kööp et al., 2016a, 2016b) and are characterized by the largest range of ^{50}Ti anomalies with $\epsilon^{50}\text{Ti}$ values ranging from -700 to 2700 (e.g., Zinner et al., 1986; Hinton et al., 1987; Ireland, 1988; Liu et al., 2009; Kööp et al., 2016a). Note that the SHIBs tend to have smaller ^{50}Ti anomalies than PLACs (e.g., Kööp et al., 2018). The rare FUN inclusions are similar to hibonite-rich inclusions in that they exhibit lower initial $^{26}\text{Al}/^{27}\text{Al}$ ratios (e.g., Park et al., 2017). However, FUN samples have ^{50}Ti anomalies that typically fall in the middle of the range of values reported for hibonite-rich inclusions and normal CAIs. Previous work has suggested that the isotopic differences between all of these refractory inclusions could be due to different formation times whereby the PLACs formed first followed by FUN inclusions, SHIBs, and then normal CAIs (e.g., Kööp et al., 2016a; Render et al., 2019; Torrano et al., 2019). In this scenario, the groups of refractory inclusions each record a different step of the progressive homogenization of presolar material from the Sun’s parental molecular cloud. However, it has not yet been shown with isotopic dating that the PLACs are in fact older than FUN inclusions, SHIBs, and normal CAIs. Therefore, the relationship between these different objects remains unknown.

In order to elucidate the relationship between these early-formed objects, it is important to understand the carriers of the isotopic anomalies. However, thus far, the only confirmed presolar carrier of isotopically anomalous material are nanospinel that show large enrichments in ^{54}Cr (Dauphas et al., 2010; Qin et al., 2011a). Given that coarse-grained normal CAIs have undergone partial or complete melting and thus, homogenization of their components, these samples are less likely to preserve any original presolar carriers. On the other hand, fine-grained CAIs—including fluffy Type A inclusions—are thought to represent condensates from a hot solar gas upon cooling and, as they have been subject to less post-condensation equilibration, could preserve signatures of their original components. Moreover, recent studies have provided evidence for internal CAI isotope heterogeneity, suggesting that some of the original building components of fine-grained CAIs survived their formation processes (Simon et al., 2017; Myojo et al., 2018; Charlier et al., 2021). For example, Simon et al. (2017) utilized laser ablation multi-collector inductively coupled plasma mass spectrometry (LA-MC-ICPMS) and reported variable ^{50}Ti anomalies in different portions of the same fine-grained CAI. Similarly, Myojo et al. (2018) reported variable ^{84}Sr anomalies in different CAI phases from a fluffy Type A inclusion. Both studies suggest that different CAI mineral phases have variable Ti and Sr isotopic anomalies in fine-grained and fluffy Type A CAIs. Additionally, recent work has presented noble gas *s*-process (i.e., slow neutron capture process of

nucleosynthesis) isotopic enrichments in the fine-grained “Curious Marie” CAI and attributed the isotopic anomalies to the presence of silicon carbide (SiC), a presolar grain formed in the outflows of asymptotic giant branch (AGB) stars, contained within the CAI (Pravdivtseva et al., 2020). Given that presolar grains are not expected to survive in the CAI-forming region/process due to the prevailing high temperatures (>1200 K, Scott and Krot, 2014), it is unclear if the SiC was incorporated into the original condensate grains or alternatively, if the SiC was present in the region where fine-grained CAIs were agglomerated. If further isotopic evidence for the presence of SiC in CAIs is obtained, this would have important implications for CAI formation, including the building materials of CAIs and how fine-grained inclusions incorporated SiC grains. Additionally, if evidence is found for specific CAI minerals hosting the isotopically anomalous material such as hibonite grains, this could provide information about the relationship between hibonite-rich inclusions and normal CAIs.

The refractory element titanium (Ti) has five stable isotopes (^{46}Ti , ^{47}Ti , ^{48}Ti , ^{49}Ti , and ^{50}Ti) and is present in refractory inclusions at the weight percent level, making it useful for understanding the origin of nucleosynthetic isotope anomalies in hibonite-rich inclusions and normal CAIs—hereafter referred to simply as CAIs. Furthermore, the Ti isotope compositions of numerous hibonite-rich inclusions and CAIs from CV, CK, CM, CO, CR, and ordinary chondrites have been reported (Niederer et al., 1980, 1981, 1985; Niemeyer and Lugmair, 1981, 1984; Heydegger et al., 1982; Ireland et al., 1985; Fahey et al., 1985, 1987; Zinner et al., 1986; Hinton et al., 1987; Ireland 1988, 1990; Papanastassiou and Brigham, 1989; Sahijpal et al., 2000; Leya et al., 2009; Trinquier et al., 2009; Williams et al., 2016; Kööp et al., 2016a, 2016b, 2018; Simon et al., 2017; Ebert et al., 2018; Davis et al., 2018; Render et al., 2019; Torrano et al., 2019). These studies have shown that most inclusions have anomalous Ti isotope compositions, however, the magnitude of the Ti isotope anomaly strongly depends on the type of inclusion investigated (*i.e.*, PLACs, SHIBs, FUN CAIs, CAIs). It is currently not known whether the variable Ti isotopic anomalies reported in CAIs are ultimately derived from incorporation of presolar grains or are representative of heterogeneity in the solar protoplanetary disk or its parental molecular cloud as a whole.

Two main approaches have been utilized to investigate the Ti isotope compositions of refractory inclusions. The first is *in-situ* studies employing either secondary ion mass spectrometry (SIMS) to investigate hibonite-rich inclusions (*e.g.*, Ireland, 1990; Liu et al., 2009; Kööp et al., 2016a, 2016b, 2018) or LA-MC-ICPMS for single spot ablation and point analyses of CAIs or CAI minerals (Williams et al., 2016; Simon et al., 2017). The second approach is chemical dissolution that yield Ti isotopic compositions of bulk CAIs utilizing MC-ICPMS (*e.g.*, Leya et al., 2009; Trinquier et al., 2009; Davis et al., 2018; Ebert et al., 2018; Render et al., 2019; Torrano et al., 2019). Some of these studies were able to measure smaller sized refractory inclusions ($<1\text{mm}$) by micro-milling the samples from the chondritic meteorites (Ebert et al., 2018; Render et al.,

2019). However, the first approach with SIMS has relatively large uncertainties compared to the latter approach, making it difficult to place constraints on the relationship between hibonite-rich inclusions and CAIs (*e.g.*, Render et al., 2019), and the second method analyzes the bulk composition of CAIs, representing an average composition that does not distinguish between different CAI phases. Consequently, important information about the individual phases present in CAIs is lost.

Another approach that elucidates the carriers of isotope anomalies is sequential acid leaching of primitive bulk meteorites (*e.g.*, Rotaru et al., 1992; Dauphas et al., 2002; Schönbacher et al., 2005; Reisberg et al., 2009; Trinquier et al., 2009; Yokoyama et al., 2010; Hidaka and Yoneda, 2011; Qin et al., 2011b; Burkhardt et al., 2019). Sequential acid leaching dissolves the various sample phases by increasing the acid strength in each step. For example, phases such as sulfates, sulfides, and carbonates are dissolved early in the leaching procedure with acetic acid, dilute HCl, and dilute HNO_3 solutions (Rotaru et al., 1992). In comparison, phases such as oxides and silicates are dissolved later in the leaching procedure when more concentrated mixtures of HF, HCl, and HNO_3 are employed. While sequential acid leaching has been used on primitive meteorites, including the Orgueil and Murchison chondrites that have internal Ti isotope heterogeneity (Trinquier et al., 2009; Burkhardt et al., 2019), this method has not been utilized for primitive CAIs.

In this study, we use two different methodologies on separate sample sets to assess the presolar carrier(s) of the Ti isotope anomalies in CAIs. The first approach is examining 15 CAIs of variable sizes from CV3 chondrites with LA-MC-ICPMS to probe different Ti-bearing CAI mineral phases. Some large CAIs were specifically selected for this work to search for internal CAI Ti isotope variations. For this purpose, Type A CAIs, especially fluffy Type A, are of particular interest as these objects are believed to have never been molten and have the most refractory compositions. The second approach is sequential acid leaching of four CAIs from CV3 chondrites, including a fluffy Type A inclusion and one fine-grained inclusion, in order to chemically separate the various Ti-bearing phases in each individual CAI. This combined CAI Ti isotopic dataset is then used to infer the cause of Ti isotope heterogeneity in the CAI-forming region/process and the implications this has for the composition of Ti-bearing solids in the solar parental molecular cloud.

2. SAMPLES AND METHODS

2.1. *In-situ* approach

2.1.1. Samples investigated

A petrologically diverse set of CAIs was selected for Ti isotope analyses utilizing laser ablation (Table 1). All CAIs originated from CV3 chondrites, but differ significantly in their sizes, textures, and mineralogy. Twelve CAIs from Allende were investigated including Type A, fluffy Type A, Type B, Type B1, Type B2, fine-grained, and a forsterite-bearing Type B. Also, we examined several CAIs

Table 1
CAI samples from CV3 chondrites for LA-MC-ICPMS.

CAI	Host meteorite	Mineral phases	Description
SJ101 ^a	Allende	gro, mel, an, cpx, fo-, cpx-rich bands, sp, and, ne	FoB
AL4884 ^a	Allende	mel, grsm, sp, an	Type B1
Bocce Ball ^b	Allende	mel, grsm, an, sp	Type B2
EK5-2-1R ^a	Allende	hib, pv, sp, mel, sod, ne	Type A – CG
461 3B3 ^a	Allende	sp, hib, mel	FG
461 13B ^a	Allende	hib, sp	Type A – FG
L144A	Leoville	mel, px, pv, sp	compact Type A
Crucible ^a	NWA 2364	grsm, mel, an, sp	Type B
MKJ1	Allende	mel, grsm, sp	fluffy Type A
MKJ2	Allende	sp, mel	FG
KAM J1	Allende	mel, grsm, sp, hib	Type B1
KAM L1	Allende	mel, pv, grsm, sp, hib	Type B
KAM L2B	Allende	mel, grsm, an, pv, sp	Type B
KAM L2F	Allende	Ca-px, an, sod, ne, hd, sp, gro	fluffy Type A
E44	Efremovka	an, mel, px	Type B1

^a Sample originally investigated in [Simon et al. \(2017\)](#).

^b This CAI is also known as American Museum of Natural History (AMNH) AL4947 and = andradite; an = anorthite; cpx = clinopyroxene; fo = forsterite; grsm = grossmanite; gro = grossular; hd = hedenbergite; hib = hibonite; mel = melilite; ne = nepheline; pv = perovskite; px = pyroxene; sod = sodalite; sp = spinel; CG = coarse-grained; FG = fine-grained; FoB = forsterite-bearing.

derived from other CV3 chondrites including a Type B CAI from Northwest Africa (NWA) 2364, a Type B1 from Efremovka, and a compact Type A CAI from Leoville. The ⁵⁰Ti anomalies for six of these inclusions (*i.e.*, EK5-2-1R, AL4884, 461 3B3, 461 13B, SJ101, and Crucible) have previously been reported by [Simon et al. \(2017\)](#), which also contains detailed information regarding the texture and mineralogy of these specific CAIs. Below we describe the other CAIs and provide a summary of all CAIs in [Table 1](#).

AMNH AL4947 is a Type B2 CAI from Allende. Nicknamed and hereafter referred to as Bocce Ball due to its spherical shape, the inclusion is ~6 mm in diameter. Petrographically, it has coarse-grained crystals of melilite, grossmanite, anorthite, and spinel in a fine-grained matrix. There are also porous regions of alteration minerals that appear to be replacing melilite. Outside the coarse-grained region of the CAI, there is a mixture of grossmanite and melilite of varying size and angularity. A thin Wark-Lovering (WR) rim up to 20 μm surrounds the object.

L144A is a compact Type A, oval-shaped CAI from Leoville and measures about 10 × 6 mm. It has fine-grained intergrown melilite and rare Ti-Al-rich pyroxene that encloses abundant micron-sized perovskite grains. Spinel is present throughout the CAI. The WL rim is composed of an inner layer of spinel, hibonite, melilite, and calcic pyroxene. The outer layer is composed predominantly of Al-rich pyroxene. The TiO₂ content of the pyroxenes varies from 2 to 7 wt% for grains near the rim and up to 17–19 wt% for interior grains ([Simon et al., 2005](#)). E44 is a Type B1 CAI from Efremovka and contains melilite, anorthite, and fassaitic pyroxene ([Young et al., 2005](#)).

461 13B is a fine-grained inclusion, originally investigated in [Simon et al. \(2017\)](#), containing hibonite and spinel within its aggregate interior ([Fig. 1a](#)). MKJ1 from Allende is a fluffy Type A CAI that is ~2.5 × 5 mm. The object has abundant Al-rich melilite which is anhedral to subhedral in

shape. Grossmanite and spinel are associated with seemingly independently rimmed objects that results from the intertwining of matrix and CAI material. MKJ2 is ~2.5 × 4 mm and forms a pseudo rectangular shape, which is in part due to how the piece was broken off from a larger slab. This CAI is fine-grained and its mantle is somewhat diffuse. The core consists mainly of spinel with a predominately melilite mantle. It appears that this CAI experienced significant alteration.

KAM J1 is an oval-shaped Type B1 CAI from Allende. The mantle is predominately melilite. The core contains grossmanite, spinel, and some hibonite. It measures ~4 × 3 mm in size. KAM L1 is an irregularly-shaped Type B CAI containing a large mantle of melilite, perovskite, and grossmanite, with a core rich in spinel and hibonite. The object measures ~4.5 × 2 mm. KAM L2B is an elongated Type B CAI, ~4 × 1 mm in size. The object contains melilite, grossmanite, anorthite, and perovskite. Spinel is concentrated on one side of the object, perhaps suggesting deformation. KAM L2F is a fluffy Type A CAI measuring ~3 × 1.5 mm ([Fig. 1b](#)). The object contains Ca-pyroxene, anorthite, sodalite, nepheline, and hedenbergite with minor amounts of spinel and grossular.

For the samples prepared at the University of California Los Angeles (UCLA), segments of chondrite containing individual CAIs were cut from larger slabs or rock fragments using a diamond blade saw. Thick sections of all samples were mounted in epoxy. To ensure that the sample surfaces were flat and adequate for analyses, the mounts were first polished using sandpaper and then a series of diamond slurries, decreasing in grit size with each subsequent step. The final step of the polishing regimen uses a ¼ micron grit size. After each day of analyses, samples were repolished with the ¼ micron grit diamond slurry to remove any material remaining on the surface due to laser ablation and ensure that the surface is flat for future analyses.

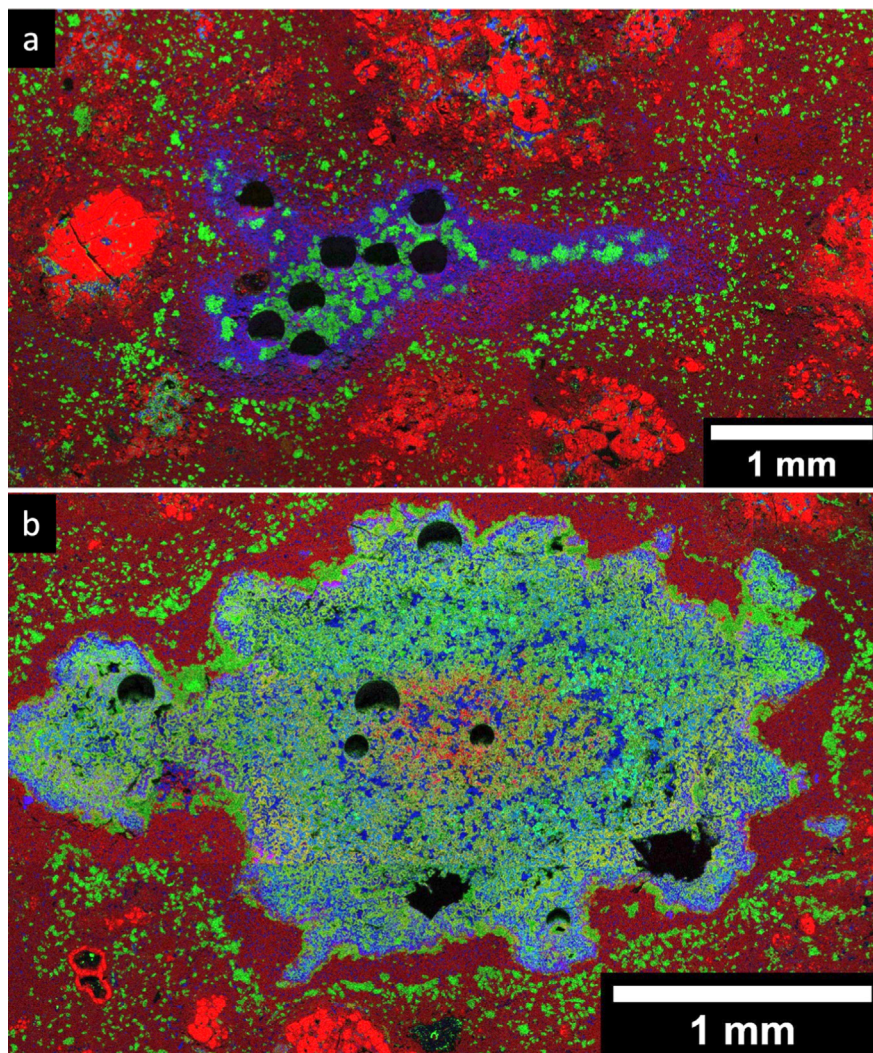


Fig. 1. False color (RGB = Mg-Ca-Al) X-ray scanning electron microscope images of (a) fine-grained CAI 461 13B and (b) fluffy Type A CAI KAM L2F. CAI 461 13B is composed of hibonite and spinel as well as hedenbergite, ferro-akermanite, and nepheline. CAI KAM L2F is composed mainly of Ca-pyroxene, anorthite, sodalite, nepheline, and hedenbergite. Circular spots are the laser ablation pits. CAI 461 13B was originally investigated in [Simon et al. \(2017\)](#).

2.1.2. Rare earth element measurements

Concentrations of rare earth elements were obtained with the CAMECA ims 1290 at UCLA following procedures previously published by [Schmitt and Vazquez \(2006\)](#). Energy-filtering was employed to suppress oxide interferences for the heavy REE. Intensities were normalized to $^{30}\text{Si}^+$. Relative sensitivity factors were obtained from analysis of NIST SRM 610 glass.

2.1.3. LA-MC-ICPMS

In-situ Ti isotope analyses were conducted at UCLA using LA-MC-ICPMS (ThermoFinnegan Neptune™) following previously published methods ([Simon et al., 2017](#)). The 193 nm excimer laser (Photon-Machines, Analyte 193) was operated at a UV of 28 J/cm² to extract Ti from the sample. Titanium measurements were predominately made in Ti-rich pyroxene with perovskite and hibonite sometimes present in the analyzed area. Material was

ablated at a pulse repetition rate of 3–6 Hz, using a spot size ranging from 86 to 172 μm depending upon the concentration of Ti. Helium (0.29 l/min) carried ablated material from the sample chamber to a mixing chamber where it combines with Ar (0.6 l/min) and N₂ (8 ml/min) before being introduced into the ICP torch. Faraday collectors with 10¹¹ Ω resistors were spaced to collect $^{47}\text{Ti}^+$, $^{49}\text{Ti}^+$, $^{50}\text{Ti}^+$, $^{51}\text{V}^+$, and $^{52}\text{Cr}^+$. The mass resolving power was ~ 7000 and standard-sample bracketing was used to correct for instrumental mass bias. Additionally, an instrumental mass fractionation factor, α_{inst} , was calculated following [Simon et al. \(2017\)](#). An individual measurement encompasses 10 cycles of 4 s integrations. We peak stripped interferences from ^{50}Cr and ^{50}V by monitoring ^{52}Cr and ^{51}V during each analysis and correcting for instrumental fractionation in the usual way (β exponents characterizing instrumental fractionation). Anomalous $^{50}\text{Ti}/^{47}\text{Ti}$ isotope effects are reported utilizing the ϵ -notation, or parts per

ten thousand deviation relative to terrestrial $^{50}\text{Ti}/^{47}\text{Ti}$. The external reproducibility of the method ($2 \times$ standard deviation, 2SD) based on multiple analyses of our UCLA Glass #5 (P10) was ± 3.7 for $\epsilon^{50}\text{Ti}$. The mass-dependent Ti isotope fractionations, obtained via standard-sample bracketing, are provided in the supplement.

2.2. Acid leaching approach

2.2.1. Samples investigated

The four CAIs selected for acid leaching were extracted from carbonaceous chondrite samples provided by the Institut für Planetologie at the University of Münster. This sample set includes one fine-grained inclusion from the CV3 chondrite Acfer 082, one fine-grained inclusion from the CV3.6 chondrite Allende, one fine- to medium-grained inclusion from the CV3 chondrite Acfer 082, and one coarse-grained inclusion from the CV3 chondrite NWA 6619 (Table 2). The CAI samples were carefully extracted from their meteorite hosts using a diamond saw. The cut surfaces were polished with SiC abrasive paper, after which each CAI weighed between 37 mg and 137 mg. Next, a corundum drill was used to further remove matrix material surrounding the CAIs. Before crushing the CAI samples, they were cleaned in ethanol for ~ 10 minutes in an ultrasonic bath. Each CAI sample was then crushed into smaller pieces using an agate mortar and pestle. Given the irregular shapes of fine-grained inclusions, the CAI pieces were carefully separated from remaining chondrite matrix by hand-picking under a stereo microscope. At this point, each CAI sample was split into two fractions: one larger mass fraction to be utilized for the leaching procedure and one smaller mass fraction to be completely digested in order to obtain a bulk CAI Ti isotope composition. CAI pieces were specifically set aside for the leaching procedure and it was visually estimated that the CAI fractions used for leaching had $<5\%$ matrix material. However, to maximize the available CAI sample material, some CAI pieces with a small amount of matrix material were utilized for the bulk CAI Ti isotope work. It was visually estimated that the total amount of matrix material in the bulk CAI fraction was $<30\%$. Note that the chondrite matrix material contains significantly less Ti (<0.08 wt% Ti; Braukmüller et al., 2018) than the CAI (~ 1 wt% Ti) so that the Ti isotope composition of the bulk CAIs should not be significantly affected by such addition of matrix material. In the worst-case scenario of 30% matrix and 70% CAI, the matrix

would be contributing $\leq 3\%$ of the total Ti, rendering it insignificant at the analytical precision achieved in this study. The CAI pieces set aside for leaching and bulk Ti isotope measurements were ground into a fine powder using an agate mortar and pestle. Smaller pieces of each CAI were also saved and put into thin sections for petrographic investigation.

All four CAIs were studied by optical and electron microscopy. A JEOL 6610-LV electron microscope at the Interdisciplinary Center for Electron Microscopy and Microanalysis (ICEM) at the University of Münster was chosen to study the texture and to identify the different mineral phases for each CAI. The attached energy dispersive spectroscopy (EDS) system was used for qualitative and quantitative mineral analyses. Samples and appropriate mineral standards were measured at an acceleration voltage of 20 kV and the beam current constancy was controlled by a Faraday cup. Natural and synthetic standards from Astimex, olivine (Mg, Fe, Si), jadeite (Na), plagioclase (Al), sanidine (K), diopside (Ca), rutile (Ti), chromium-oxide (Cr), rhodonite (Mn), and pentlandite (Ni) were used for mineral analyses. The EDS analyses were done with the INCA analytical program provided by Oxford Instruments.

Warrior, from the CV3 chondrite Acfer 082, is an irregularly-shaped and fine-grained inclusion comparable to fluffy Type A CAIs (Fig. 2a). The interior mainly consists of melilite including large areas of hibonite and spinel. Perovskite is present within melilite, spinel, and hibonite. Platy and lath-shaped hibonite (which are similar in composition) often occur in association with spinel creating hibonite/spinel patches within melilite (Fig. 2b). Small areas show signs of secondary alteration (Fig. 2b), and these altered areas are rich in Al, Ca, Ti, and Si and are nearly free of Na, K, Cr, or Ni. Perovskite is still present (Fig. 2b). A clear and distinct WL rim is not present but the inclusion is rimmed by a patchy-like spinel rim often intergrown with hibonite laths.

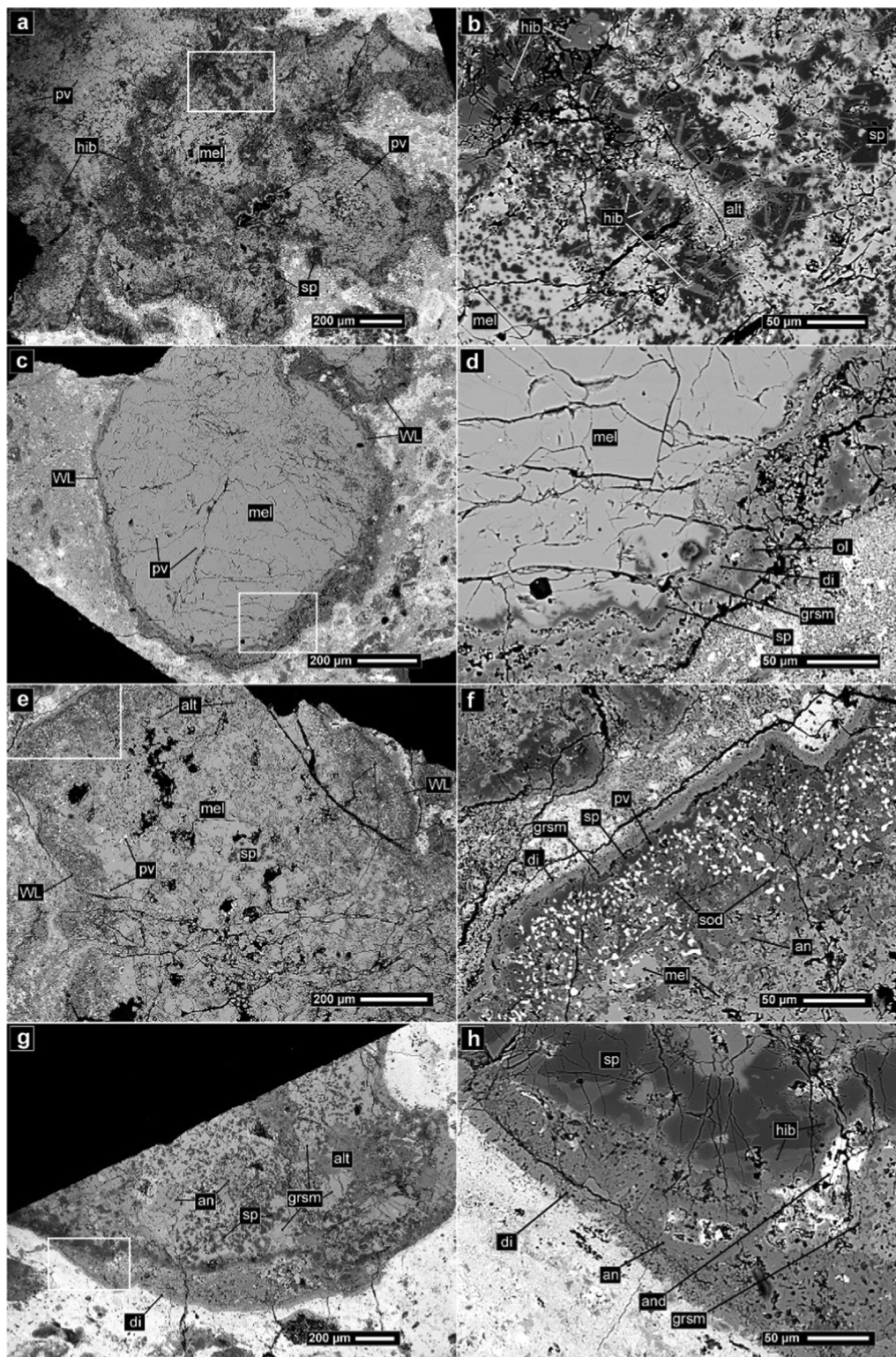
Pigeon is a fine- to medium-grained compact Type A inclusion from the CV3 chondrite Acfer 082. This CAI is dominated by melilite (>90 vol%) in the interior enclosing small perovskites (Fig. 2c). Pigeon has a very distinct WL rim consisting of (outside to inside) olivine, diopside, grossmanite, and spinel (Fig. 2d); however, in some parts of the rim the olivine is missing. Grossmanite in the rim is mostly destroyed by secondary alteration (Fig. 2d).

Lizard is a fine-grained and irregularly-shaped Type A inclusion from the CV3.6 chondrite Allende. This inclusion is dominated by melilite surrounding small grains of

Table 2
CAI samples used for acid leaching in this study.

CAI	Host meteorite	Mass for leaching (mg)	Mass for bulk Ti measurement (mg)	REE pattern	Mineral phases*	Description
Warrior	Acfer 082 (CV3)	92.5	15.8	Group III	mel, sp, hib, pv, grsm, FeNi	fluffy Type A – FG
Pigeon	Acfer 082 (CV3)	50.3	4.6	Group II	mel, di, sp, ol, grsm, pv	compact Type A – FMG
Lizard	Allende (CV3.6)	22.8	8.2	Group I	mel, di, sp, an, sod, pv, grsm	Type A – FG
Garland	NWA 6619 (CV3)	7.4	3.5	Group V	grsm, an, sp, di, hib, and	Type C – CG

* In order of high to low abundances and = andradite; an = anorthite; di = diopside; FeNi = FeNi metal; grsm = grossmanite; hib = hibonite; mel = melilite; ol = olivine; pv = perovskite; sod = sodalite; sp = spinel; CG = coarse-grained; FG = fine-grained; FMG = fine- to medium-grained.



perovskite and spinel (Fig. 2e). Secondary alteration products are present in many parts of the melilite interior. The inclusion is surrounded by a distinct WL rim consisting of (outside to inside) diopside, grossmanite, and spinel followed by a perovskite-rich layer. The area between the WL rim and dominating melilite interior is strongly affected by secondary alteration resulting in the formation of sodalite and anorthite (Fig. 2f). Furthermore, spinel in the rim is enriched in Fe (FeO ~ 4.7 wt%) relative to the spinel within the melilite of the interior (FeO ~ 1.9 wt%).

Garland is a coarse-grained Type C inclusion from the CV3 chondrite NWA 6619. This CAI mainly consists of grossmanite (present in various compositions: Al₂O₃ ~ 11.0–22.0 wt% and TiO₂ ~ 2.0–16.4 wt%) and anorthite. Furthermore, spinel is a common inclusion within both grossmanite and anorthite (Fig. 2g). Large areas are affected by secondary parent-body alteration resulting in spinel with higher concentrations of Fe than in unaffected areas. The lower part of the CAI is surrounded by a diopside rim and an “inner layer” consisting of spinel and hibonite (Fig. 2h). Both layers are missing on other parts of the CAI. This irregularly-shaped rim suggests an impact-induced fragmentation of the CAI prior to incorporation into (accretion of) the host meteorite. The area between the diopside and the spinel/hibonite rim is dominated by secondary alteration products including andradite (Fe,Si,Ca-rich phase; Fig. 2h). This phase may originate from aqueous alteration on the parent-body (Krot et al., 2008). The alteration phases closer to the center of the CAI are enriched in potassium and nickel (K₂O ~ 3.1 wt%; NiO ~ 8.2 wt%; Na₂O ~ 1.2 wt%; FeO ~ 1.4%), whereas the alteration products between the diopside and spinel rim are enriched in sodium (K₂O ~ 1.2 wt%; NiO ~ 2.8 wt%; Na₂O ~ 5.5 wt%; FeO ~ 2.3%). This speaks for two different alteration events and/or a chemically evolving fluid with time.

2.2.2. Leaching of the CAIs

The CAI powders as well as a blank were processed through a sequential acid leaching procedure modified after Reisberg et al. (2009). As the CAI samples were all less than 100 mg, in this work we used significantly less acid volume compared to the original procedure from Reisberg et al.

(2009) that was used to leach 16.5 g of the Murchison meteorite. Our sixth leaching step was similar to the adjustment made in the leaching procedure from Shollenberger and Brennecke (2020). The steps are as follows:

- Step 1) 0.9 mL acetic acid + 0.9 mL H₂O, 1 day, 20 °C.
- Step 2) 0.6 mL HNO₃ + 1.2 mL H₂O, 5 days, 20 °C.
- Step 3) 0.83 mL HCl + 0.97 mL H₂O, 1 day, 75 °C.
- Step 4) 0.9 mL HF + 0.45 mL HCl + 0.45 mL H₂O, 1 day, 75 °C.
- Step 5) 0.9 mL HF + 0.9 mL HCl, 3 days, 150 °C.
- Step 6) 0.6 mL HNO₃ + 1.2 mL HF + 34 µL HClO₄, 180 °C, 5 days.

Dry down at 180 °C to remove HClO₄.

Treat sample with 200 µl concentrated HNO₃.

Dry down at 200 °C to remove HClO₄ (repeat HNO₃ addition and dry down four times).

1.2 mL HNO₃ + 0.6 mL HCl, 2 days, 150 °C.

When the leaching was complete, all six leaching steps for each CAI and blank were evaporated to dryness at 90 °C. Subsequently, all leaching samples were treated with 3 mL of reverse aqua regia and fluxed for 1 hour at 110 °C. In preparation for chemical separation of Ti, the samples were evaporated to dryness and converted to nitride form by fluxing in 1 mL of 12 M HNO₃ at 120 °C. The samples were evaporated to dryness and brought up in 3 mL of 12 M HNO₃ and fluxed overnight at 120 °C. After letting the samples cool to room temperature, 2% of each solution was removed for analysis of major and trace element concentrations.

2.2.3. Chemical dissolution of bulk CAIs

The powdered CAI sample aliquots set aside for the bulk Ti isotope measurements were digested on hot plates in 5 mL of a 3:1 concentrated HF-HNO₃ mixture at 180 °C. After three days, 10 µL of HClO₄ was added to the samples and they were placed back on the hot plate at 180 °C for five days. The samples were evaporated to dryness and the dry down procedure previously described in Section 2.2.2 was used to remove all HClO₄. Then the samples were fluxed in 3 mL of reverse aqua regia overnight at 110 °C. The next day the samples were briefly placed in an ultra-sonic bath to physically break up grain conglomer-

Fig. 2. Backscatter electron (BSE) images of the CAIs used for acid leaching. Regions outlined in white boxes on “a, c, e, g” are shown in detail in “b, d, f, h”, respectively. (a) Warrior is a fine-grained fluffy Type A CAI that mainly consists of spinel, hibonite, and perovskite embedded in a melilite main mass. (b) Warrior close up of spinel/hibonite patches within melilite. (c) Pigeon is a compact Type A CAI and melilite is the dominant phase along with minor perovskite grains and some altered areas. (d) A distinct Wark-Lovering rim is present in Pigeon, consisting of olivine, diopside, grossmanite, and spinel. (e) Lizard is a fine-grained Type A CAI and the groundmass consists of melilite with minor spinel and perovskite. (f) Lizard is surrounded by a clear Wark-Lovering rim (from outside to inside: diopside, grossmanite, spinel followed by a mixture of perovskite with melilite including secondary alteration phases like sodalite and anorthite). (g) Garland is a coarse-grained Type C CAI and mainly consists of grossmanite, anorthite, and spinel. Garland is largely affected by secondary alteration resulting in various alteration products (enriched in potassium and nickel) and Fe-bearing spinel. (h) A diopside rim is partly present in Garland as well as an “inner rim” consisting of spinel and hibonite. The area between the two “rims” is strongly affected by secondary alteration resulting in the formation of andradite and alteration phases enriched in sodium. mel = melilite; sp = spinel; hib = hibonite; pv = perovskite; alt = alteration; grsm = grossmanite; an = anorthite; and = andradite; sod = sodalite; di = diopside; ol = olivine; WL = Wark-Lovering-rim.

ations further and then fluxed for ~4 hours at 130 °C on the hot plate. The temperature of the hot plate was increased to 150 °C overnight and the samples were fluxed for two more days to achieve complete dissolution. In preparation for chemical separation and purification of Ti, the CAI samples were evaporated to dryness, dissolved in 2 mL of 12 M HNO₃, fluxed for 1 hour at 130 °C, and evaporated to dryness at 110 °C. This step was repeated again to fully convert the samples to nitride form. Finally, the samples were dissolved in 3 mL of 12 M HNO₃ and placed on a hot plate overnight at 120 °C. Similar to the leaching solutions, 2% of each bulk CAI solution was removed for major and trace element measurements.

2.2.4. Chemical separation of Ti

We used previously described methods for the chemical purification of Ti (Zhang et al., 2011; Torrano et al., 2019). Our two-step Ti purification method utilized procedure 2 column 1 from Torrano et al. (2019) followed by column 2 from Zhang et al. (2011). The day before loading samples on the first Ti column, approximately 30–50 mg of H₃BO₃ was added to each sample solution for the complexation of fluorides and the samples were then fluxed overnight at 120 °C.

Here we briefly describe the chemical separation procedures as specific details can be found in the aforementioned studies (Zhang et al., 2011; Torrano et al., 2019). First, the dissolved samples were loaded onto pre-cleaned and pre-conditioned TODGA resin (2 mL cartridges) in 3 mL of 12 M HNO₃. The matrix was eluted in 10 mL of 12 M HNO₃ and subsequently Ti and iron (Fe) were eluted together in 10 mL of 6 M HNO₃. The Ti and Fe cut was evaporated to dryness and then fluxed in 2 mL of concentrated HNO₃. In preparation for the second column, the sample solutions were evaporated to dryness, fluxed in ~1 mL 4 M HF, evaporated to dryness, and then fluxed in 3 mL of 4 M HF. The sample solutions were loaded onto 0.8 mL of pre-cleaned and pre-conditioned Biorad AG1-X8 200–400 mesh resin (chloride form). The matrix was eluted in 10 mL of 4 M HF followed by the elution of any remaining vanadium in 10 mL of 0.4 M HCl – 1 M HF. A purified Ti cut was eluted using 5 mL of 9 M HCl – 0.01 M HF. In preparation for isotopic measurement, the purified Ti cuts were fluxed in ~1 mL concentrated HNO₃, evaporated to dryness, and fluxed in 1 mL of the running solution (*i.e.*, 0.34 M HNO₃ – 0.0014 M HF). The chemical yields for Ti through this separation procedure were typically greater than 90%. Before isotopic measurement, pre-dilutions of all samples were checked to verify that interfering elements (*i.e.*, Ca, Cr, and V) were below the maximum thresholds determined by Zhang et al. (2011) [*i.e.*, Ca/Ti ≪ 20, Cr/Ti ≪ 0.1, V/Ti ≪ 2].

2.2.5. Major and trace element measurements

Aliquots of the leaching solutions and bulk CAI samples set aside for major and trace element analysis were diluted appropriately with 2% HNO₃. Select major and trace element concentrations were obtained on a Thermo Scientific® XSeries2 quadrupole inductively coupled plasma mass spectrometer (ICP-MS) housed at the University of

Münster following previously published methods (*e.g.*, Shollenberger and Brennecka, 2020).

2.2.6. Ti isotope measurements

The Ti isotope compositions of the bulk CAIs, CAI leachates, and standards were measured at the University of Münster using a Neptune Plus MC-ICPMS in combination with a Cetac Aridus II® desolvator with jet sample and X skimmer cones following previously published methods (Gerber et al., 2017; Render et al., 2019). All samples, geological reference materials, and the bracketing Origins Lab OL-Ti standard solution were measured at Ti concentrations of 200 ppb. The Ti isotope data were reduced offline and isobaric interferences on Ti isotopes were corrected from signals monitored on masses 44 (Ca), 51 (V), and 53 (Cr). The interference corrections were well within the range that can be accurately corrected. To account for the fact that instrumental mass bias of these interfering elements can diverge from that of Ti (*e.g.*, β^{Ca} ≠ β^{Ti}, where β is the exponent characterizing instrumental fractionation), the natural isotope ratios for these interfering elements (⁴⁶Ca/⁴⁴Ca, ⁴⁸Ca/⁴⁴Ca, ⁵⁰V/⁵¹V, and ⁵⁰Cr/⁵³Cr) were manually adjusted using doped standard solution tests (Zhang et al., 2011). To verify the accuracy and reproducibility of our method, the geological reference materials BCR-2 and JB-2 were measured during the same analytical session as all samples.

To obtain mass-independent Ti variations (*i.e.*, nucleosynthetic anomalies), instrumental mass bias was corrected by internal normalization using ⁴⁹Ti/⁴⁷Ti = 0.749766 and the exponential law. The Ti isotope results are presented using the ε-notation, or parts per ten thousand deviation from the Origins Lab OL-Ti standard using the following equation where *i* represents either 46, 48, or 50:

$$\varepsilon^i \text{Ti}_{\text{sample}} = \left(\frac{({}^i\text{Ti}/{}^{47}\text{Ti})_{\text{sample}}}{({}^i\text{Ti}/{}^{47}\text{Ti})_{\text{OL-Ti standard}}} - 1 \right) \times 10,000$$

The external reproducibility of the method (2SD) based on multiple analyses of BCR-2 and JB-2 was ±0.31 for ε⁴⁶Ti, ±0.11 for ε⁴⁸Ti, and ±0.33 for ε⁵⁰Ti. The six blank measurements corresponding to each leaching step all contained <3 ng Ti, which is negligible considering most samples had significantly more than 1000 ng of Ti. The mass-dependent Ti isotope fractionations, obtained via standard-sample bracketing, are provided in the supplement.

3. RESULTS

3.1. Rare earth element patterns

Shown in Fig. 3 are the rare earth element (REE) patterns of the four bulk CAIs used for the acid leaching procedure and one CAI investigated via LA-MC-ICPMS. The REE patterns are normalized to CI chondrites (Lodders, 2003). The CAIs Lizard and Garland have mostly flat, unfractionated REE patterns, although Garland is more depleted in the heavy REEs compared to the light REEs.

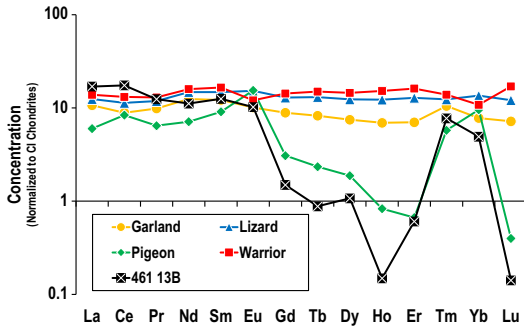


Fig. 3. Rare Earth element patterns of select CAIs analyzed in this study. Data normalized to CI chondrites using [Lodders \(2003\)](#).

On the other hand, three of the CAIs have fractionated REE patterns: Pigeon and 461 13B are characterized by the high-temperature volatility fractionation group II REE pattern whereas Warrior has depletions in europium and ytterbium consistent with the group III REE pattern.

3.2. Ti contents in the CAI leaching fractions

Shown in [Fig. 4](#) is the distribution of Ti among the six leaching steps for each individual CAI. The majority of

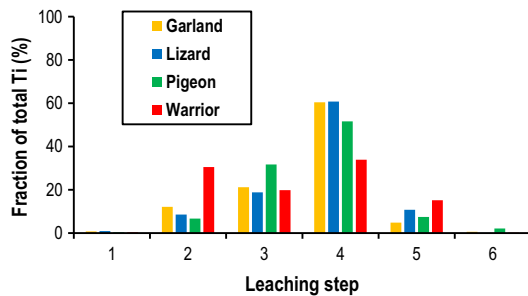


Fig. 4. The distribution of Ti in the six leaching steps shown in % for the four different CAIs. For all CAIs, significantly less Ti is liberated in the first and sixth leaching steps compared to the four middle leaching steps.

Table 3
Average ^{50}Ti anomalies of CAI samples measured via LA-MC-ICPMS.

Sample	Description	<i>n</i>	$\epsilon^{50}\text{Ti}$	\pm
<i>fine-grained/fluffy Type A</i>				
461 3B3*	FG	13	7.6	9.2
461 13B*	Type A – FG	7	41.2	13.3
MKJ2	FG	5	7.5	11.9
KAM L2F	fluffy Type A	3	4.0	4.8
MKJ1	fluffy Type A	6	-0.1	17.2
<i>coarse-grained</i>				
EK5-2-1R*	Type A – CG	6	1.0	1.8
L144A	compact Type A	27	7.7	5.4
KAM J1	Type B1	3	5.3	6.6
AL4884*	Type B1	6	8.8	4.2
E44	Type B1	5	8.8	4.1
Bocce Ball	Type B2	6	6.2	9.6
KAM L1	Type B	7	7.5	4.5
KAM L2B	Type B	5	9.0	1.0
Crucible*	Type B	1	6.5	3.7
SJ101*	FoB	5	11.0	3.3

The uncertainties shown are the $2 \times$ standard deviation (2SD) of the sample measurements or the external reproducibility of the method (2SD) for samples that were measured less than 3 times. Note that the uncertainties are substantially larger for fine-grained/fluffy Type A samples, indicating isotopic heterogeneity in these samples beyond the analytical precision of our method (see [Fig. 5a](#)). *Data for SJ101, AL4884, EK5-2-1R, 461 3B3, 461 13B, and Crucible were previously published in [Simon et al. \(2017\)](#). Note 461 3B3 was analyzed here three more times so the average value has been updated from [Simon et al. \(2017\)](#).

the Ti for each CAI is leached during steps 2–5 while only small amounts of Ti are leached in the first and sixth leaching steps ([Fig. 4](#)). Furthermore, the CAIs have different Ti release patterns. For example, Pigeon, Garland, and Lizard have a similar pattern where the amount of Ti released increases from step one to step four followed by a decrease of Ti released in the fifth and sixth steps. In contrast, Warrior has a more uniform release of Ti between the second and fifth leaching steps.

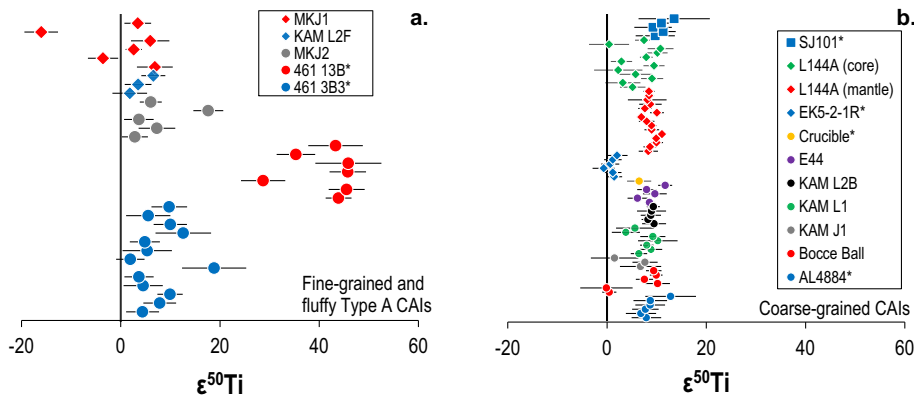


Fig. 5. The $\epsilon^{50}\text{Ti}$ spot analyses of the CAIs obtained via LA-MC-ICPMS for (a) fine-grained (circles) and fluffy Type A CAIs (diamonds) and (b) coarse-grained CAIs (Type B = circles, Type A = diamonds, forsterite bearing = squares). Uncertainties shown represent $2 \times$ standard error (2SE) internal precision of the individual measurements. *Data for SJ101, AL4884, EK5-2-1R, 461 3B3, 461 13B, and Crucible were previously published in [Simon et al. \(2017\)](#).

3.3. ^{50}Ti anomalies of CAIs via LA-MC-ICPMS

The ^{50}Ti anomalies of the 15 CAIs from CV3 chondrites are presented in Fig. 5 relative to USNM 83191 rutile (terrestrial) standard and are separated into fine-grained/fluffy Type A CAIs (Fig. 5a) and coarse-grained CAIs (Fig. 5b). The average ^{50}Ti anomalies for each CAI are located in Table 3, while data for individual spot analyses are provided in the supplementary material. The majority of the $\epsilon^{50}\text{Ti}$ values are between 6 and 10 (Fig. 5), consistent with previously reported values for CAIs (e.g., Leya et al., 2009; Trinquier et al., 2009; Williams et al., 2016; Simon et al., 2017; Davis et al., 2018; Ebert et al., 2018; Render et al., 2019; Torrano et al., 2019). The coarse-grained CAIs of this study define a range of $\epsilon^{50}\text{Ti}$ compositions from ~ -1 to 15 (Fig. 5b). In contrast, the fine-grained and fluffy Type A CAIs span a larger range of $\epsilon^{50}\text{Ti}$ compositions from ~ -16 to 45 (Fig. 5a). Furthermore, we observe intra-CAI variation in $\epsilon^{50}\text{Ti}$ for some of the samples (Fig. 5), although the widest variability is observed within the fine-grained

and fluffy Type A CAIs. For example, six different spot analyses were performed on the fluffy Type A inclusion MKJ 1 and the two most extreme $\epsilon^{50}\text{Ti}$ values were -16.0 ± 3.4 and 6.9 ± 3.6 (Fig. 5a). L144A, another compact Type A CAI, displays some variability within its core but not its mantle (Fig. 5b). The spot analyses for the mantle are tightly clustered around $\epsilon^{50}\text{Ti} = 9$ while the core displays a larger variance among data points and has a lower average value of $\epsilon^{50}\text{Ti} = 6$. Our observation of intra-CAI ^{50}Ti variation is in contrast to a previous study that did not observe any intra-CAI variation in ^{50}Ti outside of the analytical uncertainty (Williams et al., 2016).

3.4. Ti isotope compositions of CAIs and CAI leachates via solution MC-ICPMS

The Ti isotope compositions for the CAIs of this study and their corresponding leachates as well as the terrestrial basalts analyzed alongside the CAIs are provided in Table 4. The terrestrial basalts have Ti isotope compositions that are

Table 4
Titanium isotope compositions of bulk CAIs, CAI leachates, and terrestrial standards measured via solution MC-ICPMS.

Sample	Description	Host meteorite	<i>n</i>	$\epsilon^{46}\text{Ti}$	\pm	$\epsilon^{48}\text{Ti}$	\pm	$\epsilon^{50}\text{Ti}$	\pm
BCR-2	Terrestrial basalt		12	0.05	0.16	0.06	0.13	-0.13	0.34
JB-2	Terrestrial basalt		14	-0.05	0.38	0.02	0.09	-0.06	0.31
Basalt average				-0.01	0.06	0.04	0.02	-0.10	0.07
External reproducibility (2SD)					0.31		0.11		0.33
Garland bulk	Type C/CG	NWA 6619	5	1.66	0.17	0.37	0.06	9.28	0.19
L1			2	1.67	0.44	0.70	0.11	9.20	0.33
L2			5	1.73	0.18	0.41	0.08	9.30	0.29
L3			5	1.86	0.19	0.45	0.16	9.44	0.26
L4			5	1.79	0.23	0.64	0.16	9.32	0.25
L5			6	1.90	0.13	0.26	0.19	9.54	0.15
L6			2	1.89	0.31	0.33	0.21	9.11	1.88
Warrior bulk	fluffy Type A/FG	Acfer 082	9	-0.07	0.09	0.24	0.20	2.39	0.09
L1			5	-0.19	0.08	0.34	0.08	0.69	0.16
L2			7	-0.14	0.16	0.49	0.19	1.98	0.23
L3			7	-0.29	0.17	0.54	0.18	2.09	0.25
L4			8	-0.21	0.18	0.38	0.24	2.03	0.10
L5			7	-0.22	0.18	0.68	0.08	1.81	0.18
L6			5	-0.37	0.23	0.58	0.06	2.05	0.29
Pigeon bulk	compact Type A/FMG	Acfer 082	5	1.81	0.28	0.74	0.28	9.28	0.19
L1			5	1.62	0.10	0.42	0.14	8.86	0.11
L2			6	1.67	0.17	0.42	0.23	9.17	0.17
L3			6	1.78	0.27	0.45	0.10	9.25	0.14
L4			11	1.61	0.06	0.36	0.09	9.40	0.09
L5			5	2.00	0.38	0.47	0.05	9.51	0.15
L6			5	2.03	0.17	0.69	0.39	9.39	0.23
Lizard bulk	Type A/FG	Allende	5	1.79	0.10	0.49	0.04	9.53	0.28
L1			5	1.74	0.19	0.37	0.09	9.01	0.28
L2			5	1.75	0.07	0.54	0.11	9.45	0.21
L3			5	1.79	0.16	0.56	0.13	9.45	0.21
L4			5	1.76	0.17	0.53	0.16	9.53	0.26
L5			5	1.81	0.15	0.51	0.07	9.51	0.10
L6			1	1.63	0.31	0.53	0.11	9.58	0.33

Data are internally normalized to $^{49}\text{Ti}/^{47}\text{Ti} = 0.749766$. The uncertainties shown represent the 95% confidence intervals for samples that were measured 5 or more times. For samples that were measured less than 5 times, the uncertainties shown are either the external reproducibility of the method or the $2 \times$ standard deviation (2SD) of the sample measurements, whichever was larger. L1 = leachate 1, L2 = leachate 2, L3 = leachate 3, L4 = leachate 4, L5 = leachate 5, L6 = leachate 6, CG = coarse-grained, FMG = fine to medium-grained, FG = fine-grained.

indistinguishable from values reported in the literature within the analytical uncertainties (e.g., [Trinquier et al., 2009](#); [Zhang et al., 2011](#); [Davis et al., 2018](#); [Render et al., 2019](#); [Torrano et al., 2019](#)), demonstrating the accuracy of our measurements. The Ti isotope compositions of the four bulk CAIs and their six individual leachates are presented in [Fig. 6](#) relative to the OL-Ti standard. All bulk

CAIs and their leachates have $\epsilon^{46}\text{Ti}$, $\epsilon^{48}\text{Ti}$, and $\epsilon^{50}\text{Ti}$ values that are consistent with literature CAI Ti isotope data from ordinary, CM, CO, CV, and CK chondrites (e.g., [Trinquier et al., 2009](#); [Leya et al., 2009](#); [Williams et al., 2016](#); [Ebert et al., 2018](#); [Davis et al., 2018](#); [Render et al., 2019](#); [Torrano et al., 2019](#)). The bulk CAIs and their leachates have small but resolvable excesses in $\epsilon^{48}\text{Ti}$ ranging from 0.24 to 0.74 ([Fig. 6b](#)). Garland, Pigeon, Lizard, and their corresponding leachates have excesses in $\epsilon^{46}\text{Ti}$ and $\epsilon^{50}\text{Ti}$ around 1.7 and 9.4, respectively ([Fig. 6a/c](#)). In contrast, Warrior and its leachates are characterized by small deficits in $\epsilon^{46}\text{Ti}$ of ~ 0.2 and excesses in $\epsilon^{50}\text{Ti}$ of ~ 2 with the exception of the first Warrior leachate that has $\epsilon^{50}\text{Ti} = 0.69 \pm 0.16$ ([Fig. 6a/c](#)).

4. DISCUSSION

4.1. ^{50}Ti anomalies in CV3 CAIs via LA-MC-ICPMS

The 15 CV3 CAIs investigated utilizing LA-MC-ICPMS show significant ^{50}Ti variability both within and amongst CAIs ([Fig. 5](#)). The widest variability is observed in the fine-grained and fluffy Type A inclusions that are thought to represent primitive condensates from a hot solar gas upon cooling ([Fig. 5a](#)). This observation is consistent with other studies that have shown that fine-grained/fluffy Type A CAIs span a larger range of isotope anomalies compared to coarse-grained CAIs for elements like Mo ([Burkhardt et al., 2011](#); [Brennecke et al., 2020](#)) and Sr (e.g., [Myojo et al., 2018](#); [Charlier et al., 2019](#)). Evidently, the fact that fine-grained/fluffy Type A inclusions have not been melted results in the preservation of larger variations in isotopic anomalies for various elements. In contrast, the smaller range of ^{50}Ti anomalies for coarse-grained CAIs ([Fig. 5b](#)) apparently reflects the fact that these inclusions have been partially or completely melted during which their original components were equilibrated (i.e., homogenized).

Most of the CAIs investigated via laser ablation in this work tend to have $\epsilon^{50}\text{Ti}$ values clustering around 6–10 ([Fig. 5](#)) and define an average of ~ 9 . Interestingly, L144A displays variability in its core but not in the mantle ([Fig. 5b](#)). This result is consistent with the mineralogy of this CAI as the mantle is more uniform mineralogically compared to the core. Furthermore, there are CAIs with

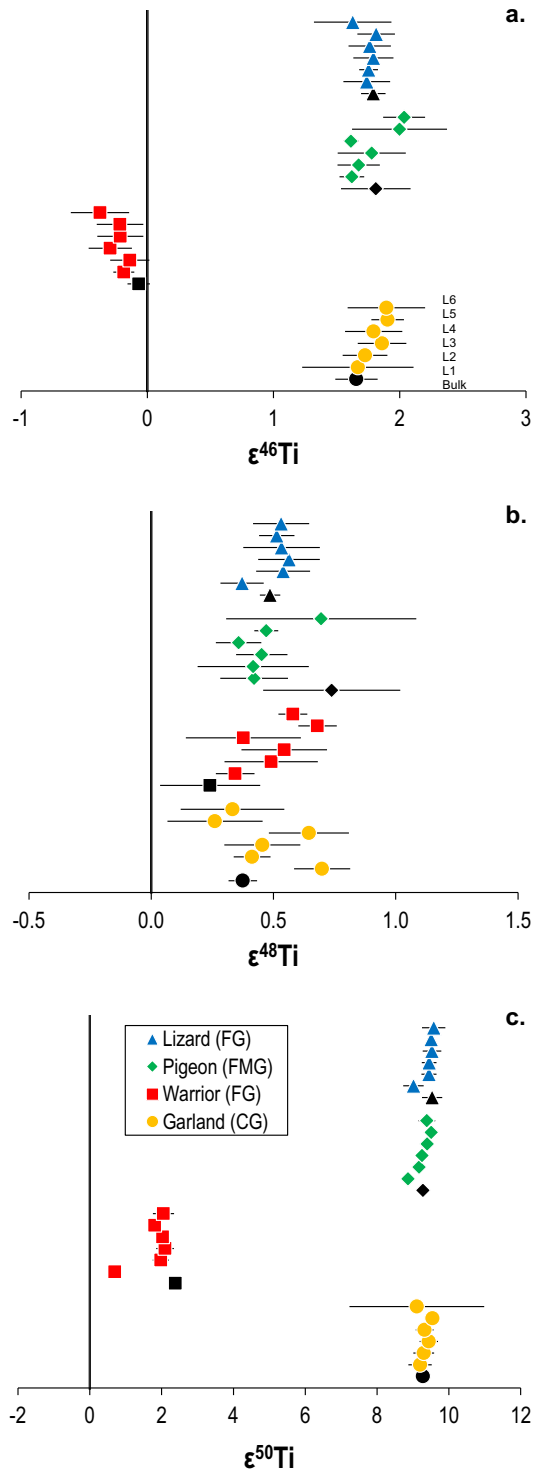


Fig. 6. The (a) $\epsilon^{46}\text{Ti}$, (b) $\epsilon^{48}\text{Ti}$, and (c) $\epsilon^{50}\text{Ti}$ data of the four CAIs and their leachates. For each CAI, the bottom data point (black) is the bulk CAI measurement. The sample directly above the bulk data point is the first leaching step followed by the second leaching step and sequentially progressing to the sixth leaching step at the top for each CAI as demonstrated by the labeling next to Garland. Data are internally normalized using the exponential law and $^{49}\text{Ti}/^{47}\text{Ti} = 0.749766$. The uncertainties shown represent the 95% confidence intervals for samples that were measured 5 or more times. For samples that were measured less than 5 times, the uncertainties shown are either the external reproducibility of the method or the 2SD of the sample measurements, whichever was larger. CG = coarse-grained, FMG = fine to medium-grained, FG = fine-grained.

more extreme $\epsilon^{50}\text{Ti}$ values such as MKJ1 and 461 13B. MKJ1 is a fluffy Type A inclusion and displays both negative and positive $\epsilon^{50}\text{Ti}$ values ranging from -16.0 ± 3.4 to 6.9 ± 3.6 . Although the most positive value is consistent with $\epsilon^{50}\text{Ti}$ isotope data from bulk CAIs, the most negative value of MKJ 1 is rare in bulk CAIs. However, a similarly negative $\epsilon^{50}\text{Ti}$ value (-18.44 ± 0.42) has been previously reported for a hibonite-rich CAI (JW-4) from the CM chondrite Jbilet Winselwan (Render et al., 2019). On the other hand, 461 13B has the largest $\epsilon^{50}\text{Ti}$ values reported for any normal CAI ranging from 28.7 ± 4.5 to 45.9 ± 6.7 (Simon et al., 2017). This CAI is a Type A fine-grained inclusion composed mainly of spinel and hibonite grains. Additionally, this inclusion has a group II REE pattern (Fig. 3), indicative of condensation from a gas fractionated previously by partial evaporation, resulting in a dearth of the more refractory REE in the gas and its condensates (e.g., Hu et al., 2021). The mineralogy and REE pattern suggest that 461 13B is a more pristine sample. Nonetheless, the fact that some of the CAIs fall significantly outside of the average $\epsilon^{50}\text{Ti}$ CAI value indicates that there was heterogeneity in the precursor material from which the CAIs formed (Brennecka et al., 2020).

4.2. Ti isotope anomalies in CV3 CAIs and their acid leachates

The Ti isotope compositions of the four bulk CAIs of this study (Fig. 6; black symbols) are variable yet fall within previously reported ranges for CAIs separated from CV, CK, CO, CM, and ordinary chondrites (e.g., Trinquier et al., 2009; Leya et al., 2009; Ebert et al., 2018; Davis et al., 2018; Render et al., 2019; Torrano et al., 2019). As previous work has suggested, the similar Ti isotopic compositions recorded by all of these CAIs indicates that these samples have a shared genetic heritage and likely formed contemporaneously in a single region of the solar nebula or from a single reservoir (e.g., Ebert et al., 2018; Render et al., 2019; Torrano et al., 2019). As such, the acid leachates derived from the four bulk CAIs of this study are also representative of CAIs in general.

In comparison to previous work in which bulk CAIs were analyzed (e.g., Leya et al., 2009; Trinquier et al., 2009; Davis et al., 2018; Ebert et al., 2018; Render et al., 2019; Torrano et al., 2019), the acid leaching procedure utilized in this work allows for the chemical separation of various Ti-bearing phases within a CAI. The acid leachates from the two coarse-grained CAIs (Pigeon and Garland) have little, if any, Ti isotope variability between the six different leaching steps for each individual CAI, as expected (Fig. 6). Given that these two CAIs were once molten, the homogenization of Ti isotopes between the various Ti-bearing phases of these inclusions is expected. On the other hand, fine-grained CAIs did not experience melting and could potentially preserve their original components. However, we observe that the two fine-grained inclusions (Warrior and Lizard) also have little, if any, Ti isotope variability between the six different leaching steps with the exception of the first Warrior leachate for $\epsilon^{50}\text{Ti}$ (Fig. 6c).

Within CAIs, Ti is mainly located in hibonite, perovskite, and pyroxene. These phases are expected to be attacked and dissolved in the middle leaching steps, and our leaching results indicate that the bulk of the Ti is released in leaching steps two through five for all four CAIs (Fig. 4). The Ti release patterns demonstrate that the major Ti-bearing phases are attacked to some extent in the second and third leaching steps and are fully dissolved once the use of HF is employed in the fourth and fifth leaching steps. This is supported by the fact that for all CAIs investigated, the most Ti is released in the fourth leaching step when HF is first used (Fig. 4). In contrast to the middle leachates, <1% of the total Ti is released in the first acid leaching step for each individual CAI (Fig. 4). This is consistent with the fact that acetic acid, which is used in the first leaching step, is not expected to dissolve any of the major Ti-bearing phases. In the final leaching step, the amount of the total Ti released is low (<3%; Fig. 4), and it is expected that the most chemically resistant phases would be attacked including spinel and SiC, if it is present in CAIs. Nevertheless, even though the CAIs selected for this work are different in terms of their mineralogy (Fig. 2) and REE patterns (Fig. 3), all acid leachates of each individual CAI have mostly uniform ^{46}Ti , ^{48}Ti , and ^{50}Ti isotope anomalies that are consistent with their corresponding bulk CAI (Fig. 6). The exception to this observation is that for all CAI samples the first leaching step has a slightly smaller ^{50}Ti anomaly compared to the middle leaching steps (Fig. 6c). Given that the first leaching step utilizes acetic acid, we interpret the smaller ^{50}Ti anomalies in the first acid leachates to be due to the dissolution of easily accessible, isotopically less anomalous Ti in CAIs hosted in alteration phases such as carbonates, sulfates, and phosphates.

4.3. Comparison between laser ablation and acid leaching

One clear difference between our two approaches, performed on separate CAI sample sets, is that the laser ablation data provides significant evidence of intra-CAI heterogeneity while the leachate data does not. The lack of variation in the Ti isotope compositions of the CAI acid leachates likely reflects that the leaching procedure itself is not effective in separating the different Ti-bearing phases compared to the laser technique. For example, all of the hibonite grains are likely to be attacked and dissolved during the same leaching steps, resulting in the average Ti isotope composition of all the hibonites that were attacked/dissolved during that step. Burkhardt et al. (2019) noted that sequential acid leachates obtained on the Murchison meteorite show only marginally larger Ti isotope anomalies compared to the range covered by bulk meteorites and CAIs, indicating that the leaching procedure was less effective in separating the anomalous Ti carrier phases. A similar observation was made on sequential acid leachates from Orgueil (Trinquier et al., 2009). As such, the lack of variation between the different leaching steps of the fine-grained CAIs does not require that the CAIs lack intra-CAI Ti isotope heterogeneity, but rather suggests that this leaching procedure is unable to efficiently separate the various Ti-bearing phases. However, only two fine-grained CAIs were

leached in this work and they may not be a completely representative population of fine-grained CAIs. Nonetheless, the laser can target specific CAI phases resulting in the observed intra-CAI ^{50}Ti isotope heterogeneity. Additionally, two CAIs, 461 3B3 and EK5-2-1R, had been previously analyzed for their ^{50}Ti isotope compositions using thermal ionization mass spectrometry (TIMS) as reported in Simon et al. (2017). For both inclusions, the ^{50}Ti TIMS data and average of the ^{50}Ti laser ablation data (Table 3) agree within the 2SD uncertainties demonstrating that both analytical methods yield consistent and accurate isotopic compositions.

Despite the lack of intra-CAI Ti isotope variability in the CAI acid leachates, we do observe Ti isotope heterogeneity amongst the different CAIs investigated. For exam-

ple, while most of the samples have similar excesses in ^{46}Ti , ^{48}Ti , and ^{50}Ti , the fluffy Type A CAI Warrior and its corresponding leachates exhibit deficits in ^{46}Ti as well as smaller excesses in ^{50}Ti (Fig. 6). To compare our data with previous work, we show in Fig. 7 plots of $\epsilon^{46}\text{Ti}$ versus $\epsilon^{50}\text{Ti}$ and $\epsilon^{48}\text{Ti}$ versus $\epsilon^{50}\text{Ti}$. In both diagrams, the bulk CAI data from this study plot on or close to linear regressions previously reported for 46 Allende CAIs (Davis et al., 2018). In agreement with previous studies, the CAIs indicate a heterogeneity of Ti isotopes in the CAI-forming region or process (e.g., Simon et al., 2017; Davis et al., 2018; Ebert et al., 2018; Render et al., 2019; Torrano et al., 2019). Using the Ti isotope data of this work as well as other recent Ti isotopic studies on CAIs derived from CV, CK, CM, and CO chondrites (Leya et al., 2009; Trinquier et al., 2009;

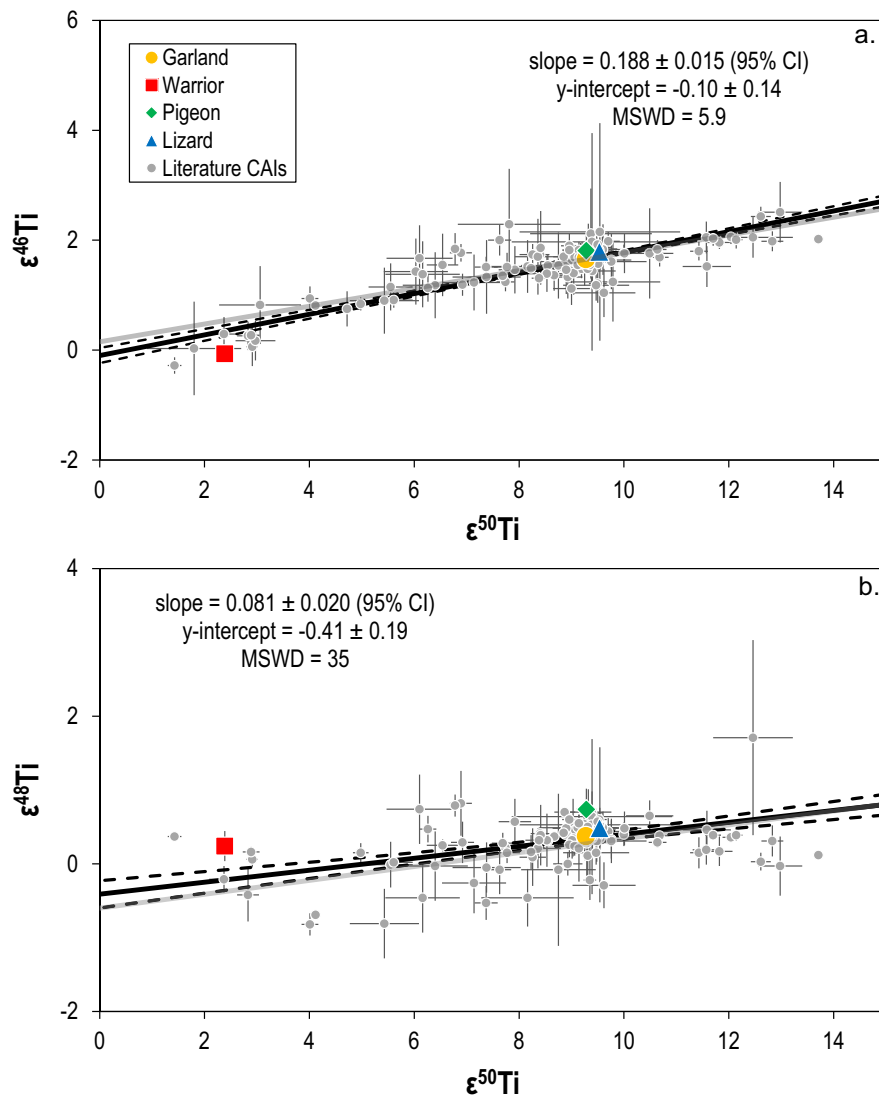


Fig. 7. (a) $\epsilon^{46}\text{Ti}$ versus $\epsilon^{50}\text{Ti}$ and (b) $\epsilon^{48}\text{Ti}$ versus $\epsilon^{50}\text{Ti}$ data of our bulk CAIs as well as literature data (shown as grey circles). Solid black lines are best-fit regressions for all CAI data, and solid grey lines are regressions reported in Davis et al. (2018) from 46 Allende CAIs, shown for comparison. Literature CAI data are from Leya et al. (2009), Trinquier et al. (2009), Davis et al. (2018), Burkhardt et al. (2019), Render et al. (2019), Torrano et al. (2019), and Brennecka et al. (2020). As indicated by high MSWDs for both regressions, there is significant scatter beyond the analytical uncertainties, suggesting the presence of multiple isotopically anomalous phases in CAIs.

Davis et al., 2018; Burkhardt et al., 2019; Render et al., 2019; Torrano et al., 2019; Brennecka et al., 2020), we recalculated the linear regression for $\epsilon^{46}\text{Ti}$ versus $\epsilon^{50}\text{Ti}$. In comparison to the slope of 0.162 ± 0.030 from Davis et al. (2018), we obtain an indistinguishable but more precise slope of 0.188 ± 0.015 (95% confidence interval, CI) for 125 CAIs (details regarding the methods and samples used to calculate these slopes and intercepts can be found in the supplementary material). Likewise, for $\epsilon^{48}\text{Ti}$ versus $\epsilon^{50}\text{Ti}$, our slope of 0.081 ± 0.020 (95% CI) for 119 CAIs is indistinguishable from the slope reported for 46 Allende CAIs (0.094 ± 0.045 ; Davis et al., 2018). Similar to Davis et al. (2018), we observe significant scatter beyond the analytical uncertainties, as indicated by $\text{MSWD} \gg 1$ for both regressions. This suggests that multiple isotopically anomalous phases are involved in the generation of Ti isotopic heterogeneity in CAIs.

4.4. On the presence of SiC in CAIs

Recent work on the Curious Marie fine-grained Allende CAI found evidence, based on *s*-process noble gas enrichments, that SiC is or was present in this particular CAI as well as three other fine-grained CAIs (Pravdivtseva et al., 2020). Pravdivtseva et al. (2020) argued that the SiC was incorporated into the CAI upon initial formation and survived later parent-body processing. However, CAIs and their precursor materials are believed to have condensed from a hot solar gas upon cooling proximal to the young sun and at such high temperatures (>1200 K), it is expected that any presolar grains like SiC would be completely destroyed by exposure to hot nebular gases (>1200 K) within ~ 1000 years (Mendybaev et al., 2002). Consistent with this, SiC grains have not yet visually been identified in any CAI. While it would be difficult to find a SiC signature in a Ti isotope measurement of a bulk CAI, the CAI acid leachates investigated in this work provide an opportunity to examine if SiC is present in CAIs. This is due to the fact that the leaching procedure is able to dissolve different CAI mineral phases in each leaching step. If present in CAIs, chemically resistant phases like SiC would be attacked in the final leaching step that utilizes the most chemically aggressive acid treatment. This has previously

been shown in leaching studies of primitive chondrites, where the last leaching step typically exhibits *s*-process enrichments, and the most likely phase responsible for the enrichments is SiC (e.g., Schönbachler et al., 2005; Qin et al., 2011b; Shollenberger & Brennecka, 2020).

The Ti isotopic compositions of various types of SiC grains—including mainstream grains—have been reported (e.g., Gyngard et al., 2018). For the purpose of this discussion, we will focus on the average Ti isotopic composition of mainstream SiC grains as they make up $\sim 90\%$ of all SiC grains (e.g., Nittler, 2003). Furthermore, mainstream SiC grains are thought to derive from AGB stars as they are characterized by large *s*-process enrichments. These grains are believed to be responsible for the *s*-process noble gas enrichments from Pravdivtseva et al. (2020). It is possible to compare the mainstream SiC Ti isotope pattern with the final leaching steps—the step that would concentrate SiC—of the four CAIs of this study (Fig. 8). When normalized to $^{49}\text{Ti}/^{47}\text{Ti}$ (Burkhardt et al., 2019), the average mainstream SiC grains are characterized by large excesses in ^{50}Ti and slightly larger excesses in ^{46}Ti (Fig. 8a). Furthermore, the mainstream SiC grains have significant deficits in ^{48}Ti . Similarly, the sixth and final acid leaching step obtained on the Murchison meteorite is characterized by deficits in ^{48}Ti accompanied by excesses in both ^{46}Ti and ^{50}Ti , although significantly smaller in magnitude compared to mainstream SiC grains (Fig. 8b; Burkhardt et al., 2019). Burkhardt et al. (2019) suggested that the first five leaching steps do not attack the chemically resistant SiC, and consequently, the sixth and final leaching step is enriched in that phase and has a Ti isotope pattern that is shifted towards a SiC pattern.

Even though the mineralogy of CAIs is different from that of whole rock Murchison, if SiC grains are present in the CAIs of this study then they would similarly shift the Ti isotope pattern in the sixth and final leaching step, given the chemically resistant nature of SiC. Therefore, in the final leaching step we would expect to see a similar pattern as that seen in the sixth Murchison leaching step characterized by deficits in ^{48}Ti and larger excesses in ^{46}Ti (Fig. 8b). However, the sixth leaching steps from the CAIs of this study have the largest excesses in ^{50}Ti followed by significantly smaller excesses in both ^{46}Ti and ^{48}Ti with the excep-

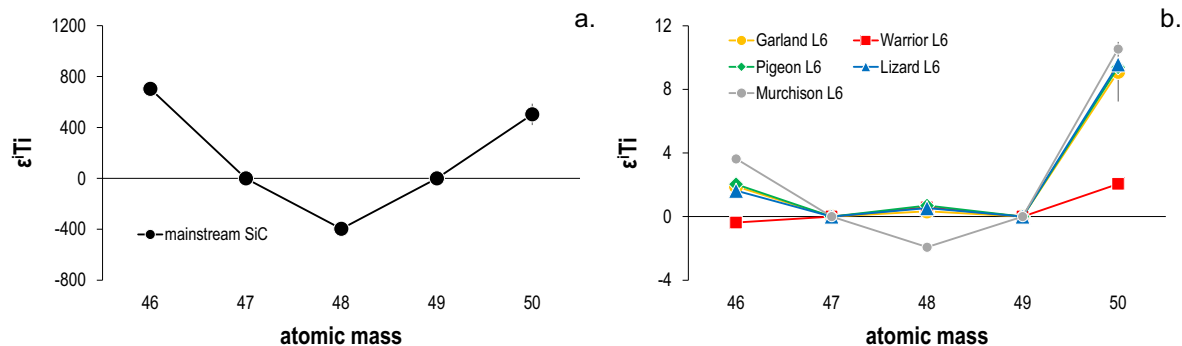


Fig. 8. Plots of the Ti isotope patterns from (a) mainstream SiC (normalized SiC grain data taken from Burkhardt et al. (2019)) and (b) the sixth leaching step of our four CAIs as well as the sixth leaching step of the Murchison meteorite from Burkhardt et al. (2019). Uncertainties for the leaching samples are smaller than the symbols with the exception of ^{50}Ti for Garland L6.

tion of the Warrior sample that has deficits in ^{46}Ti (Fig. 8b). We conclude that in our CAIs we do not observe a shift in the Ti isotope pattern for the final leaching steps due to SiC. The CAI acid leachates presented in this work suggest that SiC grains are not present in significant quantities in the CAIs of this study. This observation is contrary to the *s*-process noble gas isotopic enrichments found in fine-grained Allende CAIs that have been interpreted as a SiC signature (Pravdivtseva et al., 2020), and further work is necessary to understand the distribution of SiC in fine-grained CAIs. Although difficult to estimate, one possibility is that SiC grains contribute a significant fraction of noble gases in CAIs compared with their contribution to Ti. Titanium is much more abundant in non-presolar phases in CAIs, thus diluting any potential effects from Ti that could have been leached out of presolar phases in our CAIs. The lack of Ti isotopic evidence for SiC in CAI leachates indicates that SiC does not appear to be a major carrier phase responsible for Ti isotope anomalies in CAIs.

4.5. On the cause of Ti isotope anomalies in CAIs

The four bulk CAIs and the laser ablation spots (>100) analyzed in this work as well as bulk CAI values from the literature (>120) all demonstrate significant heterogeneity in Ti isotopes in the CAI-forming region/process. This heterogeneity is illustrated in Fig. 9 with normalized probability density plots for $\epsilon^{46}\text{Ti}$, $\epsilon^{48}\text{Ti}$, and $\epsilon^{50}\text{Ti}$. For $\epsilon^{50}\text{Ti}$, both the bulk CAI data and the laser ablation data have a well-defined probability density with a peak around 9. Prominent peaks in $\epsilon^{46}\text{Ti}$ and $\epsilon^{48}\text{Ti}$ at approximately 1.5 and 0.3, respectively, are also well-defined (Fig. 9). However, some CAIs fall outside of the main probability density peaks for each of the Ti isotope ratios, as most clearly evident in $\epsilon^{50}\text{Ti}$ (Fig. 9c). The outliers indicate that there was substantial heterogeneity in the precursor material from which the CAIs formed. For the *in-situ* work, the fine-grained CAIs, with the exception of 461 13B, form a plateau at values slightly higher than 0 for $\epsilon^{50}\text{Ti}$ (Fig. 9c). In this work, we suggest that the variable $\epsilon^{46}\text{Ti}$, $\epsilon^{48}\text{Ti}$, and $\epsilon^{50}\text{Ti}$ compositions amongst CAIs from CV, CK, CO, CM, and ordinary chondrites represent echoes of larger heterogeneities in the precursor materials that have been dampened due to averaging. However, a few notable samples such as CAIs 461 13B ($\epsilon^{50}\text{Ti} \sim 45$; Simon et al., 2017), Warrior ($\epsilon^{50}\text{Ti} \sim 2.5$), MKJ1 ($\epsilon^{50}\text{Ti} \sim 0$), JW-4 ($\epsilon^{50}\text{Ti} \sim -18$; Render et al., 2019), and JW-7 ($\epsilon^{50}\text{Ti} \sim 14$; Render et al., 2019) allow us to see this echo of precursor isotopic heterogeneity clearly. The precursor heterogeneity is likely to have been derived from solids in the parental molecular cloud.

The Ti isotopic data presented in this work as well as in previous studies suggests significant Ti isotope variability both within and amongst the genetically related CAIs from CV, CK, CM, CO, and ordinary chondrites (Fig. 9). Phases that harbor the Ti isotope anomalies in CAIs include corundum, hibonite, and perovskite, and these three phases are expected to condense in that order of descending temperature from a hot solar gas upon cooling (Ebel and Grossman, 2000). However, corundum grains contain

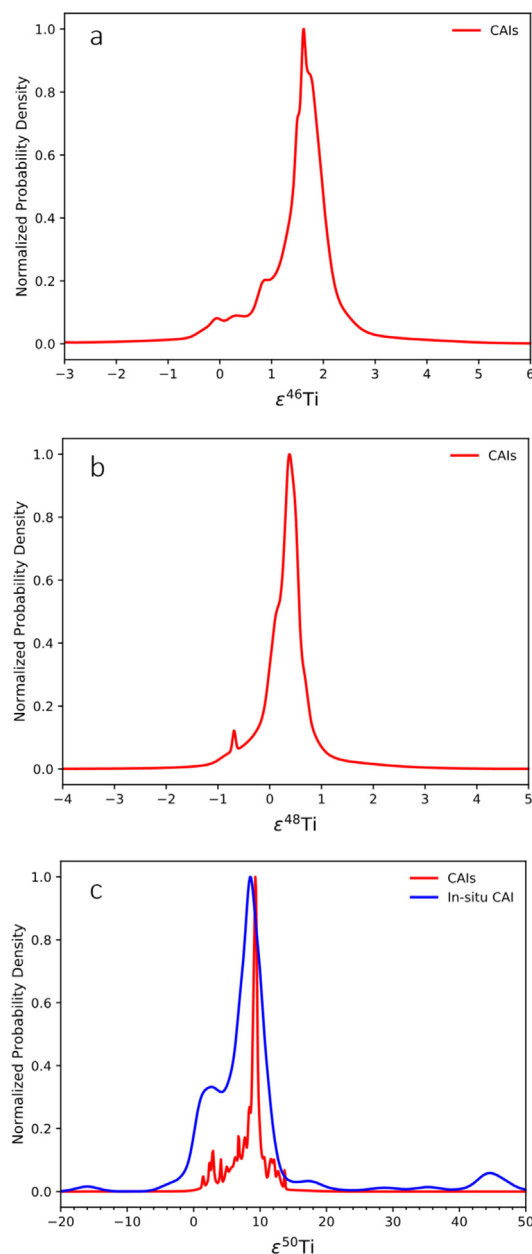


Fig. 9. Normalized probability density plots for (a) $\epsilon^{46}\text{Ti}$, (b) $\epsilon^{48}\text{Ti}$, and (c) $\epsilon^{50}\text{Ti}$ for CAIs. All isotopes of Ti display a robust probability density. Literature data are from Leya et al. (2009), Trinquier et al. (2009), Williams et al. (2016), Davis et al. (2018), Ebert et al. (2018), Shollenberger et al. (2019), Burkhardt et al. (2019), Render et al. (2019), Torrano et al. (2019), and Brennecka et al. (2020).

traces of Ti and these grains are extremely rare in CAIs (e.g., Shollenberger et al., 2018) as corundum is predicted to react with the nebular gas to form hibonite. Hibonite is more common in CAIs as a result and is an important repository for Ti. Perovskite is rich in Ti but previous work has found no correlation between perovskite content and the magnitude of the Ti isotope anomalies (Render et al., 2019). On the other hand, hibonite-rich inclusions such as SHIBS and PLACs have been shown to exhibit variable

and large Ti isotope anomalies (e.g., Zinner et al., 1986; Hinton et al., 1987; Ireland, 1988; Liu et al., 2009; Kööp et al., 2016a), making hibonite grains potential candidates for carriers of Ti isotope anomalies through to the CAI formation process. In addition, probability density functions of CAIs, SHIBs, and PLACs, all culminate close to the

same Ti isotopic compositions (Fig. 10a/b/c), indicating that Ti isotope anomalies of CAIs are purely the result of averaging large numbers of smaller SHIB and PLAC grains. The fact that PLACs and SHIBs more often than not exhibit Group II-like REE patterns, similar to those for 461 13B and Pigeon (Ireland et al., 1988), may be

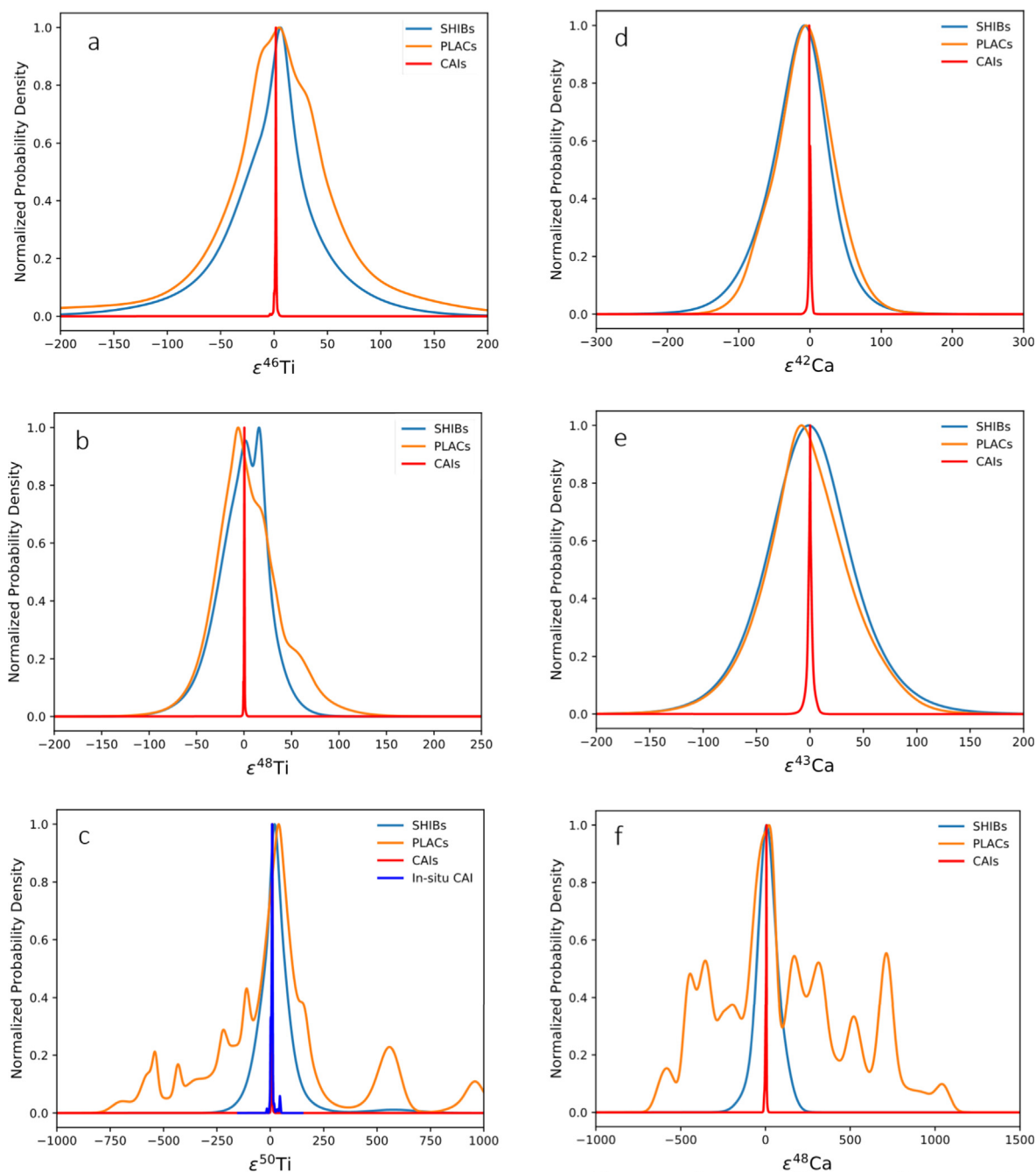


Fig. 10. Normalized probability density plots for (a) $\epsilon^{46}\text{Ti}$, (b) $\epsilon^{48}\text{Ti}$, (c) $\epsilon^{50}\text{Ti}$, (d) $\epsilon^{42}\text{Ca}$, (e) $\epsilon^{43}\text{Ca}$, and (f) $\epsilon^{48}\text{Ca}$ for hibonite-rich objects as well as CAIs. The more tightly restrained values for CAIs suggests the CAI composition reflects averaging of the isotopically diverse hibonite grains. Literature hibonite data are all renormalized Ti isotope ratios presented in Steele and Boehnke (2015) as well as data from Kööp et al. (2016a; 2018). Literature hibonite, SHIB, and CAI Ca data are from Zinner et al. (1986), Clayton et al. (1988), Ireland (1990), Ireland et al. (1991), Russell et al. (1998), Sahijpal et al. (2000), Kööp et al. (2016a, 2016b, 2018), Niederer and Papanastassiou (1979, 1984), Papanastassiou and Brigham (1989), Moynier et al. (2010), Huang et al. (2012), Chen et al. (2015), and Bermingham et al. (2018).

evidence for the influence of hibonite-rich material as precursors to the fine-grained CAIs. We note that the Group II patterns for 461 13B and Pigeon resemble those of perovskites from Murchison, including the lack of depletions in the more volatile Eu and Yb (Ireland et al., 1988).

To further examine if the averaging of hibonite grains can explain the Ti isotopic compositions of CAIs, shown in Fig. 10a/b/c are normalized probability density plots of $\epsilon^{46}\text{Ti}$, $\epsilon^{48}\text{Ti}$, and $\epsilon^{50}\text{Ti}$ for hibonite data reported in the literature. Overlain on top of these data are the CAI data from Fig. 9. For the hibonite grains, the data span a range in $\epsilon^{50}\text{Ti}$ from approximately -750 to over 1000 . The hibonite grains have smaller ranges in both $\epsilon^{46}\text{Ti}$ and $\epsilon^{48}\text{Ti}$ compared to $\epsilon^{50}\text{Ti}$. However, a main peak is observed in all three plots. The peaks for the CAIs mimic those of the hibonite grains, but are much more tightly clustered around their common peak in the probability density functions. This observation is best explained by CAIs representing averages of their precursor materials characterized by the hibonite-rich inclusions. Note that the hibonite data exhibit a skew towards higher $\epsilon^{50}\text{Ti}$ values that would explain the fact that the CAI data have relatively small but distinctly positive $\epsilon^{50}\text{Ti}$ values. Although all CAIs show an order of magnitude less dispersion in Ti isotope anomalies compared with the hibonites, the concept of an “echo” of dispersion is bolstered by the persistence of a greater spread in values among the unmelted (*i.e.*, fine-grained and fluffy Type A) CAIs. The greater spread in non-mass dependent Ti isotope ratios among the unmelted CAIs testifies to the importance of melting in the averaging process.

The effect of averaging on Ti isotope variations in CAIs can be quantified utilizing the central limit theorem. The central limit theorem requires that random sampling of a population characterized by an initial mean value and standard deviation (with replacement), results in an approximately normal distribution with a more restricted dispersion (smaller standard deviation). The central limit theorem can be expressed in terms of the dispersion in the random sample, σ' , and the original dispersion, σ , according to the equation:

$$\sigma' = \sigma(N)^{-1/2} \quad (1)$$

where N is the number of random samples taken from the parent population. In the present application σ is the standard deviation defined by the hibonites, N represents the number of hibonite grains averaged to create a CAI, and σ' is the expected standard deviation of the CAIs. Note that the original population, in this case the hibonite data, does not need to be characterized by a normal distribution for the central limit theorem to apply; the resulting population obtained by averaging will converge to normal distributions regardless. We apply the central limit theorem to $\epsilon^{46}\text{Ti}$, $\epsilon^{48}\text{Ti}$, and $\epsilon^{50}\text{Ti}$ in hibonite-rich inclusions and CAIs to test the hypothesis that the latter are averages of the former. For these calculations we take a typical CAI as having a radius of $300 \mu\text{m}$, suggesting that ~ 8000 precursor grains similar to the hibonites with radii of $15 \mu\text{m}$ are required to compose a single CAI. In the case of $\epsilon^{50}\text{Ti}$, we calculate a standard deviation of 416 for the hibonites reported in the literature (Steele and Boehnke, 2015; Kööp et al., 2016a,

Table 5

Central limit theorem (CLT) parameters and results in comparison to CAI data for averaging a mixture of $N = 8000$ hibonite grains to form a single CAI. In this context, σ is the standard deviation of Ti or Ca isotopic compositions for hibonites, σ' is the expected standard deviation of Ti or Ca isotopic compositions for a resulting sub-population of CAIs. Overall, $\sigma(\text{CAI})$ is in good agreement with the predictions from the CLT, supporting the idea that the range of Ti and Ca isotope data of CAIs result from averaging isotopically anomalous hibonite grains.

	^{46}Ti	^{48}Ti	^{50}Ti	^{42}Ca	^{43}Ca	^{48}Ca
σ	54	22	416	25	22	312
σ'	0.6	0.2	4.6	0.3	0.2	3.5
cf. $\sigma(\text{CAI})$	0.8	0.4	2.5	1.4	1.7	3.4

2018), yielding for a CAI obtained by averaging 8000 of these grains

$$\sigma'_{50\text{Ti}} = 416(8000)^{-1/2} = 4.6 \quad (2)$$

In comparison, the actual standard deviation from the CAI data is 2.5 . We take these values within a factor of 2 of one another to be evidence that the data are consistent with the central limit theorem (Table 5). These same calculations were also performed for $\epsilon^{46}\text{Ti}$ and $\epsilon^{48}\text{Ti}$ and are summarized in Table 5. For all three isotope ratios of Ti, the standard deviation of over 130 measured bulk CAI samples is consistent with the prediction from the central limit theorem based on the spread in hibonite values. We note that there are some differences between the predictions from the central limit theorem and the actual standard deviation of the CAIs. For example, the predicted dispersion among CAIs is smaller than the observed CAI standard deviations for $\epsilon^{46}\text{Ti}$ and $\epsilon^{48}\text{Ti}$ by a factor of 2 or less (Table 5). However, the differences are well within the uncertainties arising from the vagaries of the assumptions made to arrive at N in Eq. (2), for example. The factor of 2 discrepancy between the prediction and the measured $\epsilon^{50}\text{Ti}$ CAI data (Table 5) may reflect the fact that most of the CAIs analyzed for $\epsilon^{50}\text{Ti}$ are larger CAIs ($\geq 500 \mu\text{m}$) derived from CV3 chondrites. Nevertheless, the overall agreement from the CAI data and central limit theorem predictions demonstrates that the Ti isotope compositions of CAIs from CV, CK, CM, CO, and ordinary chondrites can be explained by the averaging of more isotopically diverse hibonite grains.

To further evaluate the effect of averaging hibonite grains to form CAIs, we performed the same exercise for the refractory element Ca, which is a major constituent in both CAIs and hibonite. Calcium isotopic data from hibonite-rich objects and normal CAIs from Valdes et al. (2021) are shown as normalized probability density plots for $\epsilon^{42}\text{Ca}$, $\epsilon^{43}\text{Ca}$, and $\epsilon^{48}\text{Ca}$ in Fig. 10d/e/f. For the hibonite grains, the data span a range in $\epsilon^{48}\text{Ca}$ from approximately -600 to over 1000 . The hibonite grains have smaller ranges in both $\epsilon^{42}\text{Ca}$ and $\epsilon^{43}\text{Ca}$ compared to $\epsilon^{48}\text{Ca}$. However, a main peak is observed in all three plots that coincides in each case with the peaks defined by the much more tightly clustered CAI data. Consistent with the Ti isotopic results,

this observation is best explained by CAIs representing averages of their precursor materials, vestiges of which comprise the hibonite-rich inclusions. We investigated this relationship using the central limit theorem (CLT) and the result is presented in Table 5. Overall, the predictions from the CLT are consistent with the standard deviations defined by Ca isotopic data from the literature. This demonstrates that the Ca isotope compositions of CAIs can also be explained by the averaging of more isotopically diverse hibonite grains.

Application of the central limit theorem shows that dispersion in non-mass dependent Ti and Ca isotope ratios among CAIs and hibonite grains is the natural consequence of averaging and results neither from large-scale heterogeneities in reservoirs nor from diachronous additions of nuclides to the solar system. Primary evidence for the statistical effect comes from the decrease in dispersion in various isotope ratios with increasing size. In other words, PLACs have the largest range of Ti and Ca isotope anomalies and are smaller in size compared to CAIs. CAIs, on the other hand, have the smallest range of Ti and Ca isotope anomalies and are larger in size compared to PLACs. The success of the central limit theorem in explaining the relationship between CAIs and hibonite-rich inclusions in Ti and Ca isotope ratios suggests that this may be a useful concept for other isotope systems in CAIs.

Extrapolation back to the dispersion in isotope ratios among the molecular cloud grains suggests extreme grain-to-grain variability of many orders of magnitude in these most primitive solids. We can apply the central limit theorem in reverse, working back from the hibonite population to their molecular cloud precursors. Assuming comparable densities, it takes roughly 27 million presolar grains with diameters of 0.1 μm to comprise a single 30 μm diameter hibonite. This suggests, for example, that the dispersion in $\epsilon^{50}\text{Ti}$ among presolar grains in the molecular cloud should have been on the order of 2×10^6 in epsilon units based on a spread of about 400 for $\epsilon^{50}\text{Ti}$ among the hibonites. Such large variations in $\epsilon^{50}\text{Ti}$ have been found in presolar grains, with values up to 10^5 to 10^6 in epsilon units (Jadhav et al., 2008, Nittler et al., 2018).

5. CONCLUSIONS

This study combined Ti isotopic data from *in-situ*, sequential acid leaching, and bulk dissolution techniques in order to investigate the origin of Ti isotopic anomalies in the earliest solids known to have formed in the Solar System. The *in-situ* LA-MC-ICPMS data revealed significant ^{50}Ti heterogeneity both within and amongst the diverse sample set of 15 CV CAIs investigated. Fine-grained CAIs span a larger range of ^{50}Ti anomalies compared to coarse-grained CAIs, testifying to the more primitive character of fine-grained inclusions. The ^{50}Ti anomalies recorded by the 15 CAIs in this study are consistent with previously published values from CV, CK, CM, CO, and ordinary chondrite CAIs, and provide further evidence for significant Ti isotope heterogeneity in the CAI-forming region/process.

In contrast, sequential acid leaching of two coarse-grained and two fine-grained CAIs revealed no significant

intra-CAI Ti isotope heterogeneity. The lack of intra-CAI Ti isotope heterogeneity in the acid leachates, particularly the two fine-grained inclusions, likely reflects that the leaching procedure is unable to efficiently separate the major Ti-bearing phases. As a result, each leaching step has a similar Ti isotope composition to the bulk CAI value. Furthermore, the lack of ^{48}Ti deficits as well as larger ^{46}Ti excesses in the final leaching step—the most chemically aggressive step that would attack SiC—of four leached CAIs suggests that SiC is not present in significant quantities in these CAIs. This demonstrates that SiC grains themselves are not a major phase responsible for the Ti isotope anomalies found in CAIs.

Instead, by comparing probability density functions of mass-fractionation corrected $^{46}\text{Ti}/^{47}\text{Ti}$, $^{48}\text{Ti}/^{47}\text{Ti}$, and $^{50}\text{Ti}/^{47}\text{Ti}$ ratios from CAIs, PLACs, and SHIBs, this work demonstrates that the Ti isotope anomalies of the CAI population can be explained by the averaging of isotopically diverse hibonite grains. In turn, the diverse Ti isotopic compositions of hibonite grains reflect condensation from an isotopically heterogeneous molecular cloud. This idea of averaging is additionally supported by Ca isotopic data from the literature and is quantitatively supported by the central limit theorem.

Declaration of Competing Interest

The authors declare that they have no known competing financial interests or personal relationships that could have appeared to influence the work reported in this paper.

ACKNOWLEDGEMENTS

This work was funded by a Deutsche Forschungsgemeinschaft (DFG, German Research Foundation) research fellowship (project number 440227108) to QRS and by the University of Münster. EDY acknowledges support from NASA's emerging worlds program (80NSSC19K0511). The authors thank U. Heitmann for assistance with CAI sample preparation and I. Kohl for assistance with LA-MC-ICPMS. Part of this work was performed under the auspices of the U.S. Department of Energy by Lawrence Livermore National Laboratory under contract DE-AC52-07NA27344 with release number LLNL-JRNL-826242. The authors thank J. Simon, A. Trinquier, and one anonymous reviewer for their insightful comments that enhanced the manuscript. Additionally, the authors thank L. Qin for her comments and editorial handling.

APPENDIX A. SUPPLEMENTARY MATERIAL

Supplementary data to this article can be found online at <https://doi.org/10.1016/j.gca.2022.03.001>.

REFERENCES

- Amelin Y., Kaltenbach A., Iizuka T., Stirling C. H., Ireland T. R., Petaev M. and Jacobsen S. B. (2010) U-Pb chronology of the Solar System's oldest solids with variable $^{238}\text{U}/^{235}\text{U}$. *Earth Planet. Sci. Lett.* **300**, 343–350.
- Bermingham K. R., Gussone N., Mezger K. and Krause J. (2018) Origins of mass-dependent and mass-independent Ca isotope

- variations in meteoritic components and meteorites. *Geochim. Cosmochim. Acta* **226**, 206–223.
- Braukmüller N., Wombacher F., Hezel D. C., Escoube R. and Münker C. (2018) The chemical composition of carbonaceous chondrites: Implications for volatile element depletion, complementarity and alteration. *Geochim. Cosmochim. Acta* **239**, 17–48.
- Brennecka G. A., Burkhardt C., Budde G., Kruijjer T. S., Nimmo F. and Kleine T. (2020) Astronomical context of Solar System formation from molybdenum isotopes in meteorite inclusions. *Science* **370**, 837–840.
- Budde G., Burkhardt C., Brennecka G. A., Fischer-Gödde M., Kruijjer T. S. and Kleine T. (2016) Molybdenum isotopic evidence for the origin of chondrules and a distinct genetic heritage of carbonaceous and non-carbonaceous meteorites. *Earth Planet. Sci. Lett.* **454**, 293–303.
- Burkhardt C., Kleine T., Oberli F., Päck A., Bourdon B. and Wieler R. (2011) Molybdenum isotope anomalies in meteorites: Constraints on solar nebula evolution and origin of the Earth. *Earth Planet. Sci. Lett.* **312**, 390–400.
- Burkhardt C., Dauphas N., Hans U., Bourdon B. and Kleine T. (2019) Elemental and isotopic variability in solar system materials by mixing and processing of primordial disk reservoirs. *Geochim. Cosmochim. Acta* **261**, 145–170.
- Charlier B. L. A., Tissot F. L. H., Dauphas N. and Wilson C. J. N. (2019) Nucleosynthetic, radiogenic and stable strontium isotopic variations in fine- and coarse-grained refractory inclusions from Allende. *Geochim. Cosmochim. Acta* **265**, 413–430.
- Charlier B. L. A., Tissot F. L. H., Vollstaedt H., Dauphas N., Wilson C. J. N. and Marquez R. T. (2021) Survival of presolar p-nuclide carriers in the nebula revealed by stepwise leaching of Allende refractory inclusions. *Sci. Adv.* **7**, abf6222.
- Chen H.-W., Lee T., Lee D.-C. and Chen J.-C. (2015) Correlation of ^{48}Ca , ^{50}Ti , and ^{138}La heterogeneity in the Allende refractory inclusions. *Astrophys. J.* **806**, L21.
- Clayton R. N., Hinton R. W. and Davis A. M. (1988) Isotopic variations in the rock-forming elements in meteorites. *Philos. Trans. Roy. Soc. London. Ser. A, Math. Phys. Sci.* **325**, 483–501.
- Connelly J. N., Bizzarro M., Krot A. N., Nordlund Å., Wielandt D. and Ivanova M. A. (2012) The absolute chronology and thermal processing of solids in the solar protoplanetary disk. *Science* **338**, 651–655.
- Dauphas N. and Schauble E. A. (2016) Mass fractionation laws, mass-independent effects, and isotopic anomalies. *Annu. Rev. Earth Planet. Sci.* **44**, 709–783.
- Dauphas N., Marty B. and Reisberg L. (2002) Molybdenum nucleosynthetic dichotomy revealed in primitive meteorites. *Astrophys. J.* **569**, L139–L142.
- Dauphas N., Remusat L., Chen J. H., Roskosz M., Papanastassiou D. A., Stodolna J., Guan Y., Ma C. and Eiler J. M. (2010) Neutron-rich chromium isotope anomalies in supernova nanoparticles. *Astrophys. J.* **720**, 1577–1591.
- Davis A. M., Zhang J., Greber N. D., Hu J., Tissot F. L. H. and Dauphas N. (2018) Titanium isotopes and rare earth patterns in CAIs: Evidence for thermal processing and gas-dust decoupling in the protoplanetary disk. *Geochim. Cosmochim. Acta* **221**, 275–295.
- Ebel D. S. and Grossman L. (2000) Condensation in dust-enriched systems. *Geochim. Cosmochim. Acta* **64**, 339–366.
- Ebert S., Render J., Brennecka G. A., Burkhardt C., Bischoff A., Gerber S. and Kleine T. (2018) Ti isotopic evidence for a non-CAI refractory component in the inner solar system. *Earth Planet. Sci. Lett.* **498**, 257–265.
- Fahey A. J., Goswami J. N., McKeegan K. D. and Zinner E. (1985) Evidence for extreme ^{50}Ti enrichments in primitive meteorites. *Astrophys. J.* **296**, L17–L20.
- Fahey A. J., Goswami J. N., McKeegan K. D. and Zinner E. (1987) ^{26}Al , ^{244}Pu , ^{50}Ti , REE, and trace element abundances in hibonite grains from CM and CV meteorites. *Geochim. Cosmochim. Acta* **51**, 329–350.
- Gerber S., Burkhardt C., Budde G., Metzler K. and Kleine T. (2017) Mixing and transport of dust in the early solar nebula as inferred from titanium isotope variations among chondrules. *Astrophys. J.* **841**, L17–L23.
- Gyngard F., Amari S., Zinner E. and Marhas K. K. (2018) Correlated silicon and titanium isotopic compositions of presolar SiC grains from the Murchison CM2 chondrite. *Geochim. Cosmochim. Acta* **221**, 145–161.
- Heydegger H. R., Foster J. J. and Compton W. (1982) Terrestrial, meteoritic, and lunar Ti isotopic ratios reevaluated: Evidence for correlated variations. *Earth Planet. Sci. Lett.* **58**, 406–418.
- Hidaka H. and Yoneda S. (2011) Diverse nucleosynthetic components in barium isotopes of carbonaceous chondrites: Incomplete mixing of s- and r-process isotopes and extinct ^{135}Cs in the early solar system. *Geochim. Cosmochim. Acta* **75**, 3687–3697.
- Hinton R. W., Davis A. M. and Scatena-Wachel D. E. (1987) Large negative ^{50}Ti anomalies in refractory inclusions from the Murchison carbonaceous chondrite: Evidence for incomplete mixing of neutron-rich supernova ejecta into the solar system. *Astrophys. J.* **313**, 420–428.
- Hu J. Y., Dauphas N., Tissot F. L. H., Yokochi R., Ireland T. J., Zhang Z., Davis A. M., Ciesla F. J., Grossman L., Charlier B. L. A., Roskosz M., Alp E. E., Hu M. Y. and Zhao J. (2021) Heating events in the nascent solar system recorded by rare earth element isotopic fractionation in refractory inclusions. *Sci. Adv.* **7**, eabc2962.
- Huang S., Farkas J., Yu G., Petaev M. I. and Jacobsen S. B. (2012) Calcium isotopic ratios and rare earth element abundances in refractory inclusions from the Allende CV3 chondrite. *Geochim. Cosmochim. Acta* **77**, 252–265.
- Ireland T. R. (1988) Correlated morphological, chemical, and isotopic characteristics of hibonites from the Murchison carbonaceous chondrite. *Geochim. Cosmochim. Acta* **52**, 2827–2839.
- Ireland T. R. (1990) Presolar isotopic and chemical signatures in hibonite-bearing refractory inclusions from the Murchison carbonaceous chondrite. *Geochim. Cosmochim. Acta* **54**, 3219–3237.
- Ireland T. R., Fahey A. J. and Zinner E. K. (1991) Hibonite-bearing microspherules: A new type of refractory inclusions with large isotopic anomalies. *Geochim. Cosmochim. Acta* **55**, 367–379.
- Ireland T. R., Compston W. and Heydegger H. R. (1985) Titanium isotopic anomalies in hibonites from Murchison carbonaceous chondrite. *Geochim. Cosmochim. Acta* **49**, 1989–1993.
- Ireland T. R., Fahey A. J. and Zinner E. K. (1988) Trace-element abundances in hibonites from the Murchison carbonaceous chondrite: Constraints on high-temperature processes in the solar nebula. *Geochim. Cosmochim. Acta* **52**, 2841–2854.
- Jacobsen B., Yin Q.-Z., Moynier F., Amelin Y., Krot A. N., Nagashima K., Hutcheon I. D. and Palme H. (2008) ^{26}Al - ^{26}Mg and ^{207}Pb - ^{206}Pb systematics of Allende CAIs: Canonical solar initial $^{26}\text{Al}/^{27}\text{Al}$ ratio reinstated. *Earth Planet. Sci. Lett.* **272**, 353–364.
- Jadhav M., Amari S., Marhas K. K., Zinner T. and Gallino R. (2008) New stellar sources for high-density, presolar graphite grains. *Astrophys. J.* **682**, 1479–1485.
- Kööp L., Davis A. M., Nakashima D., Park C., Krot A. N., Nagashima K., Tenner T. J., Heck P. R. and Kita N. (2016a) A link between oxygen, calcium and titanium isotopes in ^{26}Al -poor hibonite-rich CAIs from Murchison and implications for

- the heterogeneity of dust reservoirs in the solar nebula. *Geochim. Cosmochim. Acta* **189**, 70–95.
- Kööp L., Nakashima D., Heck P. R., Kita N. T., Tenner T. J., Krot A. N., Nagashima K., Park C. and Davis A. M. (2016b) New constraints on the relationship between ²⁶Al and oxygen, calcium and titanium isotopic variation in the early solar system from a multielement isotopic study of spinel-hibonite inclusions. *Geochim. Cosmochim. Acta* **184**, 151–172.
- Kööp L., Davis A. M., Krot A. N., Nagashima K. and Simon S. B. (2018) Calcium and titanium isotopes in refractory inclusions from CM, CO, and CR chondrites. *Earth Planet. Sci. Lett.* **489**, 179–190.
- Krot A. N., Chaussidon M., Yurimoto H., Sakamoto N., Nagashima K., Hutcheon I. D. and MacPherson G. J. (2008) Oxygen isotopic compositions of Allende Type C CAIs: Evidence for isotopic exchange during nebular melting and asteroidal metamorphism. *Geochim. Cosmochim. Acta* **72**, 2534–2555.
- Kruijer T. S., Burkhardt C., Budde G. and Kleine T. (2017) Age of Jupiter inferred from the distinct genetics and formation times of meteorites. *Proc. Natl. Acad. Sci. USA* **114**, 6712–6716.
- Leya I., Schönbächler M., Krähenbühl U. and Halliday A. N. (2009) New titanium isotope data for Allende and Efremovka CAIs. *Astrophys. J.* **702**, 1118–1126.
- Liu M.-C., McKeegan K. D., Goswami J. N., Marhas K. K., Sahijpal S., Ireland T. R. and Davis A. M. (2009) Isotopic records in CM hibonites: Implications for timescales of mixing of isotope reservoirs in the solar nebula. *Geochim. Cosmochim. Acta* **73**, 5051–5079.
- Liu M.-C., Chaussidon M., Göpel G. and Lee T. (2012) A heterogeneous solar nebula as sampled by CM hibonite grains. *Earth Planet. Sci. Lett.* **327**, 75–83.
- Lodders K. (2003) Solar system abundances and condensation temperatures of the elements. *Astrophys. J.* **591**, 1220–1247.
- MacPherson G. J. and Grossman L. (1984) “Fluffy” Type A Ca-, Al-rich inclusions in the Allende meteorite. *Geochim. Cosmochim. Acta* **48**, 29–46.
- MacPherson G. J., Kita N. T., Ushikubo T., Bullock E. S. and Davis A. M. (2012) Well-resolved variations in the formation ages for Ca-Al-rich inclusions in the early Solar System. *Earth Planet. Sci. Lett.* **331–332**, 43–54.
- Mendybaev R. A., Beckett J. R., Grossman L., Stolper E., Cooper R. F. and Bradley J. P. (2002) Volatilization kinetics of silicon carbide in reducing gases: An experimental study with applications to the survival of presolar grains in the solar nebula. *Geochim. Cosmochim. Acta* **66**, 661–682.
- Moynier F., Simon J. I., Podosek F. I., Meyer B. S., Brannon J. and DePaolo D. J. (2010) Ca isotope effects in Orgueil leachates and the implications for the carrier phases of ⁵⁴Cr anomalies. *Astrophys. J.* **718**, L7–L13.
- Myojo K., Yokoyama T., Okabayashi S., Wakaki S., Sugiura N. and Iwamori I. (2018) The origin and evolution of nucleosynthetic Sr isotope variability in calcium and aluminum-rich refractory inclusions. *Astrophys. J.* **853**, 48–56.
- Nanne J. A. M., Nimmo F., Cuzzi J. N. and Kleine T. (2019) Origin of the non-carbonaceous-carbonaceous meteorite dichotomy. *Earth Planet. Sci. Lett.* **511**, 44–54.
- Niederer F. R. and Papanastassiou D. A. (1979) Ca isotopes in Allende and Leoville inclusions. *Lunar Planet. Sci.* **10**, 913–915.
- Niederer F. R. and Papanastassiou D. A. (1984) Ca isotopes in refractory inclusions. *Geochim. Cosmochim. Acta* **48**, 1279–1293.
- Niederer F. R., Papanastassiou D. A. and Wasserburg G. J. (1980) Endemic isotopic anomalies in titanium. *Astrophys. J.* **240**, 73–77.
- Niederer F. R., Papanastassiou D. A. and Wasserburg G. J. (1981) The isotopic composition of Ti in the Allende and Leoville meteorites. *Geochim. Cosmochim. Acta* **45**, 1017–1031.
- Niederer F. R., Papanastassiou D. A. and Wasserburg G. J. (1985) Absolute isotopic abundances of Ti in meteorites. *Geochim. Cosmochim. Acta* **49**, 835–851.
- Niemeyer S. and Lugmair G. W. (1981) Ubiquitous isotopic anomalies in Ti from normal Allende inclusions. *Earth Planet. Sci. Lett.* **53**, 211–225.
- Niemeyer S. and Lugmair G. W. (1984) Titanium isotopic anomalies in meteorites. *Geochim. Cosmochim. Acta* **48**, 1401–1416.
- Nittler L. R. (2003) Presolar stardust in meteorites: Recent advances and scientific frontiers. *Earth Planet. Sci. Lett.* **209**, 259–273.
- Nittler L. R., Alexander C. M. O’ D., Niu N. and Wang J. (2018) Extremely ⁵⁴Cr- and ⁵⁰Ti-rich presolar oxide grains in a primitive meteorite: Formation in rare types of supernovae and implications for the astrophysical context of Solar System birth. *Astrophys. J.* **856**, L24–L30.
- Papanastassiou D. A. and Bringham C. A. (1989) The identification of meteorite inclusions with isotope anomalies. *Astrophys. J. Lett.* **338**, 37–40.
- Park C., Nagashima K., Krot A. N., Huss G. R., Davis A. M. and Bizzarro M. (2017) Calcium-aluminum-rich inclusions with fractionation and unidentified nuclear effects (FUN CAIs): II. Heterogeneities of magnesium isotopes and ²⁶Al in the early Solar System inferred from in situ high-precision magnesium-isotope measurements. *Geochim. Cosmochim. Acta* **201**, 6–24.
- Pravdivtseva O., Tissot F. L. H., Dauphas N. and Amari S. (2020) Evidence of presolar SiC in the Allende Curious Marie calcium-aluminum-rich inclusion. *Nat. Astron.* **4**, 617–624.
- Qin L., Nittler L. R., Alexander C. M. O’ D., Wang J., Stadermann F. J. and Carlson R. W. (2011a) Extreme ⁵⁴Cr-rich nano-oxides in the CI chondrite Orgueil – implication for a late supernova injection into the solar system. *Geochim. Cosmochim. Acta* **75**, 629–644.
- Qin L., Carlson R. W. and Alexander C. M. O’ D. (2011b) Correlated nucleosynthetic isotopic variability in Cr, Sr, Ba, Sm, Nd and Hf in Murchison and QUE 97008. *Geochim. Cosmochim. Acta* **75**, 7806–7828.
- Reisberg L., Dauphas N., Luguet A., Pearson D. G., Gallino R. and Zimmermann C. (2009) Nucleosynthetic osmium isotope anomalies in acid leachates of the Murchison meteorite. *Earth Planet. Sci. Lett.* **277**, 334–344.
- Render J., Ebert S., Burkhardt C., Kleine T. and Brennecka G. A. (2019) Titanium isotopic evidence for a shared genetic heritage of refractory inclusions from different carbonaceous chondrites. *Geochim. Cosmochim. Acta* **254**, 40–53.
- Rotaru M., Birck J. L. and Allegre C. J. (1992) Clues to early solar system history from chromium isotopes in carbonaceous chondrites. *Nature* **358**, 465–470.
- Russell S. S., Huss G. R., Fahey A. J., Greenwood R. C., Hutchison R. and Wasserburg G. J. (1998) An isotopic and petrologic study of calcium-aluminum-rich inclusions from CO₃ meteorites. *Geochim. Cosmochim. Acta* **62**, 689–714.
- Sahijpal S., Goswami J. N. and Davis A. M. (2000) K, Mg, Ti and Ca isotopic compositions and refractory trace element abundances in hibonites from CM and CV meteorites: Implications for early solar system processes. *Geochim. Cosmochim. Acta* **64**, 1989–2005.
- Schönbächler M., Rehkämper M., Fehr M. A., Halliday A. N., Hattendorf B. and Günther D. (2005) Nucleosynthetic zirconium isotope anomalies in acid leachates of carbonaceous chondrites. *Geochim. Cosmochim. Acta* **69**, 113–122.

- Scott E. R. D. and Krot A. N. (2014) Chondrites and their components. In *Meteorites and Cosmochemical Processes* (ed. A. M. Davis), Vol. 1 *Treatise on Geochemistry*, 2nd ed. (Exec. Eds. H. D. Holland and K. K. Turekian). Elsevier, Oxford. pp. 65–137.
- Schmitt A. K. and Vazquez J. A. (2006) Alteration and remelting of nascent oceanic crust during continental rupture: Evidence from zircon geochemistry of rhyolites and xenoliths from the Salton Trough, California. *Earth Planet. Sci. Lett.* **252**, 260–274.
- Shollenberger Q. R. and Brennecke G. A. (2020) Dy, Er, and Yb isotope compositions of meteorites and their components: Constraints on presolar carriers of the rare earth elements. *Earth Planet. Sci. Lett.* **529**, 115866.
- Shollenberger Q. R., Borg L. E., Render J., Ebert S., Bischoff A., Russell S. S. and Brennecke G. A. (2018) Isotopic coherence of refractory inclusions from CV and CK meteorites: Evidence from multiple isotope systems. *Geochim. Cosmochim. Acta* **228**, 62–80.
- Shollenberger Q. R., Wittke A., Render J., Mane P., Schuth S., Weyer S., Gussone N., Wadhwa M. and Brennecke G. A. (2019) Combined mass-dependent and nucleosynthetic isotope variations in refractory inclusions and their mineral separates to determine their original Fe isotope compositions. *Geochim. Cosmochim. Acta* **263**, 215–234.
- Simon J. I., Young E. D., Russell S. S., Tonui E. K., Dyl K. A. and Manning C. R. (2005) A short timescale for changing oxygen fugacity in the solar nebula revealed by high-resolution ^{26}Al - ^{26}Mg dating of CAI rims. *Earth Planet. Sci. Lett.* **238**, 272–283.
- Simon J. I., Jordan M. K., Tappa M. J., Schauble E. A., Kohl I. E. and Young E. D. (2017) Calcium and titanium isotope fractionation in refractory inclusions: Tracers of condensation and inheritance in the early solar protoplanetary disk. *Earth Planet. Sci. Lett.* **472**, 277–288.
- Steele R. C. J. and Boehnke P. (2015) Titanium isotope source relations and the extent of mixing in the proto-solar nebula examined by independent component analysis. *Astrophys. J.* **802**, 80–92.
- Trinquier A., Elliott T., Ulfbeck D., Coath C., Krot A. N. and Bizzarro M. (2009) Origin of nucleosynthetic isotope heterogeneity in the solar protoplanetary disk. *Science* **324**, 374–376.
- Torrano Z. A., Brennecke G. A., Williams C. D., Romaniello S. J., Rai V. K., Hines R. R. and Wadhwa M. (2019) Titanium isotope signatures of calcium-aluminum-rich inclusions from CV and CK chondrites: Implications for early Solar System reservoirs and mixing. *Geochim. Cosmochim. Acta* **263**, 13–30.
- Valdes M. C., Bermingham K. R., Huang S. and Simon J. I. (2021) Calcium isotope cosmochemistry. *Chem. Geol.* **581**, 120396.
- Warren P. H. (2011) Stable-isotopic anomalies and the accretionary assemblage of the Earth and Mars: A subordinate role for carbonaceous chondrites. *Earth Planet. Sci. Lett.* **311**, 93–100.
- Williams C. D., Janney P. E., Hines R. R. and Wadhwa M. (2016) Precise titanium isotope compositions of refractory inclusions in the Allende CV3 chondrite by LA-MC-ICPMS. *Chem. Geol.* **436**, 1–10.
- Yokoyama T., Alexander C. M. O' D. and Walker R. J. (2010) Osmium isotope anomalies in chondrites: Results for acid residues and related leachates. *Earth Planet. Sci. Lett.* **291**, 48–59.
- Young E. D., Simon J. I., Galy A., Russell S. S., Tonui E. and Lovera O. (2005) Supra-canonical $^{26}\text{Al}/^{27}\text{Al}$ and the residence time of CAIs in the solar protoplanetary disk. *Science* **308**, 223–227.
- Zhang J., Dauphas N., Davis A. M. and Pourmand A. (2011) A new method for MC-ICPMS measurement of titanium isotopic composition: Identification of correlated isotope anomalies in meteorites. *J. Anal. At. Spectrom.* **26**, 2197–2205.
- Zinner E. K., Fahey A. J., Goswami J. N., Ireland T. R. and McKeegan K. D. (1986) Large ^{48}Ca anomalies are associated with ^{50}Ti anomalies in Murchison and Murray hibonites. *Astrophys. J.* **311**, 103–107.

Associate editor: Liping Qin